Subgrid-scale models and large-eddy simulation of oxygen stream disintegration and mixing with a hydrogen or helium stream at supercritical pressure

EZGI S. TAŞKINOĞLU[1] AND JOSETTE BELLAN[1,2]†

[1]Mechanical Engineering Department, California Institute of Technology, Pasadena, CA 91125, USA
[2]Jet Propulsion Laboratory, California Institute of Technology, Pasadena, CA 91109, USA

For flows at supercritical pressure, p, the large-eddy simulation (LES) equations consist of the differential conservation equations coupled with a real-gas equation of state, and the equations utilize transport properties depending on the thermodynamic variables. Compared to previous LES models, the differential equations contain not only the subgrid-scale (SGS) fluxes but also new SGS terms, each denoted as a 'correction'. These additional terms, typically assumed null for atmospheric pressure flows, stem from filtering the differential governing equations and represent differences, other than contributed by the convection terms, between a filtered term and the same term computed as a function of the filtered flow field. In particular, the energy equation contains a heat-flux correction (q-correction) which is the difference between the filtered divergence of the molecular heat flux and the divergence of the molecular heat flux computed as a function of the filtered flow field. We revisit here a previous *a priori* study where we only had partial success in modelling the q-correction term and show that success can be achieved using a different modelling approach. This *a priori* analysis, based on a temporal mixing-layer direct numerical simulation database, shows that the focus in modelling the q-correction should be on reconstructing the primitive variable gradients rather than their coefficients, and proposes the approximate deconvolution model (ADM) as an effective means of flow field reconstruction for LES molecular heat-flux calculation. Furthermore, an *a posteriori* study is conducted for temporal mixing layers initially containing oxygen (O) in the lower stream and hydrogen (H) or helium (He) in the upper stream to examine the benefit of the new model. Results show that for any LES including SGS-flux models (constant-coefficient gradient or scale-similarity models; dynamic-coefficient Smagorinsky/Yoshizawa or mixed Smagorinsky/Yoshizawa/gradient models), the inclusion of the q-correction in LES leads to the theoretical maximum reduction of the SGS molecular heat-flux difference; the remaining error in modelling this new subgrid term is thus irreducible. The impact of the q-correction model first on the molecular heat flux and then on the mean, fluctuations, second-order correlations and spatial distribution of dependent variables is also demonstrated. Discussions on the utilization of the models in general LES are presented.

Key words: turbulence modelling, turbulence simulation, turbulent mixing

---

† Email address for correspondence: josette.bellan@jpl.nasa.gov

1. Introduction

The simulation of high-pressure turbulent flows, where the pressure, p, is larger than the critical value, p_c, for the species under consideration, is relevant to a wide array of propulsion systems, e.g. gas turbine, diesel and liquid rocket engines. Most turbulence models have, however, been developed for atmospheric-p turbulent flows. The difference between atmospheric-p and supercritical-p turbulence is that whereas in the former situation the coupling between dynamics and thermodynamics is moderate to negligible, for the latter situation it is very significant and can dominate the flow characteristics (Okong'o, Harstad & Bellan 2002; Okong'o & Bellan 2002a, 2004a). The reason for this fact is in the mathematical form of the equation of state (EOS), which is the perfect-gas EOS in the former case and the real-gas EOS in the latter case. The perfect gas EOS is mildly nonlinear and, with the exception of the molar mass term, is the same for all chemical species; the molar mass term does not have substantial variation in the realm of species involved in combustion reactions relevant to propulsion systems. In contrast, the Peng–Robinson (PR) EOS (Prausnitz, Lichtenthaler & de Azevedo 1986) is strongly nonlinear and does not obey the corresponding state principle, so it is species-dependent through coefficients which are strongly dependent on the critical properties and acentric factor of the species (e.g. Okong'o, Harstad & Bellan 2002), all of which exhibit considerable variation with the species. The PR EOS along with many other EOSs not obeying the corresponding state principle are of practical interest because they have been extensively tested and their range of validity is well known. These observations have important consequences for large-eddy simulations (LES) in which the conservation equations are filtered and, in order to solve the LES equations, models must be used for those filtered terms which are not directly computable from the LES solution. For atmospheric-p flows, it has been shown that the only significant filtered terms in the LES equations are the subgrid-scale (SGS) fluxes (Vreman, Geurts & Kuerten 1995; Okong'o & Bellan 2004b). However, for supercritical turbulent flows, additional terms were shown to be rivalling, and sometimes surpassing in r.m.s. magnitude the SGS-flux terms (Selle *et al.* 2007). Consistent with the strong EOS dependence on species, depending on the chemical species, different additional terms were found significant in the LES equations according to the species under consideration. For the heptane/nitrogen (HN) C_7H_{16}/N_2 mixing-layer configuration, the new prominent term was in the momentum equation: the gradient of the difference between the filtered pressure, $\overline{p}$, and p computed using the filtered flow field, $p(\overline{\phi})$. Here $\phi = \{\rho, \rho u_i, \rho e_t, \rho Y_\alpha\}$ is the vector of conservative variables where ρ is the density, u_i is the velocity component in the x_i-direction spatial coordinate, e_t is the total energy and Y_α is the mass fraction of species α. For any component of the primitive variable vector $\psi(\phi) = \{u_i, p, X_\alpha, T\}$, where X_α is the mole fraction of species α, and T is the temperature, the filtering operation is defined as

$$\overline{\psi}(\boldsymbol{x}) = G * \psi = \int_V \psi(\boldsymbol{y}) G(\boldsymbol{x} - \boldsymbol{y}) \, \mathrm{d}\boldsymbol{y}, \qquad (1.1)$$

where G is the filter function and V is the filtering volume. For the oxygen/hydrogen (OH) O_2/H_2 system, the additional prominent term was in the energy equation: the difference between the divergence of the filtered molecular heat flux, $\overline{\boldsymbol{q}(\phi)}$ and the divergence of $\boldsymbol{q}(\overline{\phi})$. For the oxygen/helium (OHe) O_2/He system, each of these terms was less important than for the HN and OH systems, respectively, but was still non-negligible compared to the corresponding resolved term in the equation (i.e. $\nabla p(\overline{\phi})$ or

$\nabla \cdot \boldsymbol{q}(\overline{\phi})$). (For none of these systems was there a substantial molecular mass diffusion term difference between the filtered quantity and the same quantity computed as a function of the filtered flow field; see table 9 of Selle *et al.* 2007.) The variation among species systems is traceable to the different EOSs for these species systems (although all EOSs had the PR form) and to the different transport properties. Physically, these additional terms were necessary to reproduce high-density-gradient magnitude (HDGM) regions distributed throughout the flow (Taşkinoğlu & Bellan 2010), as seen both in direct numerical simulations (DNS) at transitional states (Okong'o *et al.* 2002; Okong'o & Bellan 2002*a*) and in fully turbulent flow experiments (Mayer *et al.* 1996, 1998; Chehroudi, Talley & Coy 1999; Oschwald & Schik 1999; Oschwald *et al.* 1999; Segal & Polikhov 2008). This filamentary morphology of the HDGM regions is a manifestation of fluid stream disintegration (i.e. loss of integrity of the heavy-fluid stream), and it was found that in these filaments the fluid is a mixture of the heavy and light fluids due to solvability effects (Okong'o *et al.* 2002; Okong'o & Bellan 2002*a*); this situation is very different from that under atmospheric *p* where the equivalent of the HDGM regions exclusively contains the heavy fluid, as during atomization.

The additional terms in the LES equations stem from the usual 'LES assumptions' – that the difference between a filtered quantity and the same quantity computed from the filtered flow field is negligible with respect to other terms in the equation – not being satisfied. By definition, the LES assumptions are any subgrid terms originating from other than the convective terms. The fact that the LES assumptions are not satisfied is the result of strong subgrid-scale activity, which, if removed through filtering, distorts the solution from its physical counterpart. Finding of non-negligible LES-assumption terms is not restricted to supercritical flows, as has also been identified in atmospheric-*p* fully multicomponent species flows, where non-uniformities are at a finer scale than in flows containing only a small number of species (Bellan & Selle 2009). Basically, to enable LES computations, these new terms must be replaced in the LES equations with SGS models, similar in concept to the ubiquitous SGS-flux models.

For supercritical turbulent binary-species flows, the implication of the above-discussed findings is that, unlike in atmospheric-*p* binary-species turbulent flows, the type and mathematical form of SGS models may be species dependent. This SGS model dependence on species may impose a large development burden in terms of obtaining appropriate SGS models, but given the importance of the applications it should not be dismissed. For example, the accurate prediction of the heat flux to the wall is a long-standing problem in liquid rocket propulsion because of the implications it has for wall-material performance and rocket integrity. Several LES were compared to heat flux experimental data versus axial direction in Tucker *et al.* (2008) to predict single-element coaxial injector flow and combustion. The results showed that only the most computationally intensive LES, with 255×10^6 cells, requiring 2×10^6 CPU hours and the utilization of 2000 processors (on average) was closest to the experimental data, but this LES was based on classical SGS-flux models, without the additional terms we advocate. The expectation is that with the additional terms we propose, the LES grid could be made coarser because these terms would account for SGS activity that currently only a fine LES grid can resolve.

Having previously addressed the modelling of the momentum equation term in an *a posteriori* study (Taşkinoğlu & Bellan 2010), we here focus on the additional SGS term in the energy equation, with application to the OH and OHe systems. Following the presentation in §2 of the LES governing equations, the databases are summarized in §3, the LES initial and boundary conditions are presented in §4 and the LES

numerical methodology is described in §5. In §6, we first revisit the *a priori* modelling of the additional SGS term for which a model was presented in §2.4.2, given that only partial success was achieved in a previous *a priori* analysis (Selle *et al.* 2007). Results are presented in §6 by first assessing *a priori* the models presented in §2.4.2. Choosing the best model for the additional term, an *a posteriori* investigation is presented in §6.2 with the goal of reproducing in LES an approximation as close as possible to the filtered-and-coarsened (FC) DNS: filtered to remove the small scales that are not computed in LES, and coarsened to reduce the number of nodes from DNS to those of LES. Generally, the FC-DNS field can be considered as a sample of the DNS field and a typically ideal, unachievable, LES template. However, if the chosen LES grid is relatively coarse, as it must necessarily be for computational efficiency when the configuration has physically large dimensions (e.g. a rocket combustion chamber), enhancement to LES could be obtained through modelling of terms not satisfying the LES assumptions, and in the best case one may strive to achieve an LES having, from a viewpoint of specific interest, no more deficiency than FC-DNS with respect to the DNS. To assess the impact of the additional-term model, we first conduct LES without, and then with this additional term, and compare the results in §6.2. Conclusions and perspectives for using this methodology in LES are given in §7.

2. Large-eddy simulation governing equations

The LES equations were derived by Selle *et al.* (2007) from the conservation equations by spatial filtering using the filter defined in (1.1). As typical for compressible flows, Favre filtering is used, defined as $\tilde{\psi} = \overline{\rho \psi} / \bar{\rho}$. Furthermore, the variance of two quantities φ and θ is defined as $\vartheta(\varphi, \theta) = \overline{\varphi \theta} - \bar{\varphi}\,\bar{\theta}$ or $\vartheta(\varphi, \theta) = \widetilde{\varphi \theta} - \widetilde{\varphi}\widetilde{\theta}$, depending on the filtering. The governing equations are written for the conservative variable vector ϕ, and include the additional SGS term in the energy equation since it is the focus of our study.

2.1. *LES differential equations*

The LES differential equations, derived under the assumption that filtering and differentiation commute (the top-hat filter is used here for which the operations commute except near boundaries), are (Selle *et al.* 2007)

$$\frac{\partial \bar{\rho}}{\partial t} + \frac{\partial \bar{\rho}\tilde{u}_j}{\partial x_j} = 0, \tag{2.1}$$

$$\frac{\partial \bar{\rho}\tilde{u}_i}{\partial t} + \frac{\partial \bar{\rho}\tilde{u}_i\tilde{u}_j}{\partial x_j} = -\frac{\partial p(\overline{\phi})}{\partial x_i} + \frac{\partial \sigma_{ij}(\overline{\phi})}{\partial x_j} - \frac{\partial}{\partial x_j}(\bar{\rho}\tau_{ij}), \tag{2.2}$$

$$\left.\begin{aligned} \frac{\partial \bar{\rho}\tilde{e}_t}{\partial t} + \frac{\partial \bar{\rho}\tilde{e}_t\tilde{u}_j}{\partial x_j} &= -\frac{\partial p(\overline{\phi})\tilde{u}_j}{\partial x_j} - \frac{\partial q_{IKj}(\overline{\phi})}{\partial x_j} + \frac{\partial \sigma_{ij}(\overline{\phi})\tilde{u}_i}{\partial x_j}, \\ &- \frac{\partial}{\partial x_j}(\bar{\rho}\zeta_j) - \frac{\partial(\bar{\rho}\tau_{ij}\tilde{u}_i)}{\partial x_j} - \frac{\partial}{\partial x_j}[q_{IKj}(\phi) - q_{IKj}(\overline{\phi})], \end{aligned}\right\} \tag{2.3}$$

$$\frac{\partial \bar{\rho}\tilde{Y}_\alpha}{\partial t} + \frac{\partial \bar{\rho}\tilde{Y}_\alpha\tilde{u}_j}{\partial x_j} = -\frac{\partial j_{\alpha j}(\overline{\phi})}{\partial x_j} - \frac{\partial}{\partial x_j}(\bar{\rho}\eta_{\alpha j}), \tag{2.4}$$

where the SGS fluxes are

$$\tau_{ij} = \vartheta(\widetilde{u}_i, \widetilde{u}_j), \quad \zeta_j = \vartheta(\tilde{h}, \tilde{u}_j), \quad \eta_{\alpha j} = \vartheta(\widetilde{Y}_\alpha, \widetilde{u}_j) \text{ with } \sum_{\alpha=1}^{\mathcal{N}} \eta_{\alpha j} = 0, \tag{2.5}$$

and the additional SGS term is $(\nabla \cdot [\overline{q_{IKj}(\phi)} - q_{IKj}(\overline{\phi})])$. In (2.1)–(2.4), t is the time, $\boldsymbol{\sigma}$ is the viscous stress tensor, $\boldsymbol{q}_{IK}$ is the Irwing–Kirkwood (subscript IK) heat flux (Sarman & Evans 1992), $e = e_t - e_K$ is the internal energy, $e_K = u_i u_i / 2$ is the kinetic energy, $\mathcal{N}$ is the number of species and $\boldsymbol{j}_\alpha$ is the species-mass flux of species α. Conservation principles impose

$$\sum_{\alpha=1}^{\mathcal{N}} Y_\alpha = 1, \quad \sum_{\alpha=1}^{\mathcal{N}} j_{\alpha j} = 0. \tag{2.6}$$

The Einstein summation is used for Roman indices (i, j, k), but not for Greek indices (α, β). The thermodynamic variables are functions of the LES flow field $\overline{\phi}$:

$$e = e(\overline{\phi}), \quad p = p(\overline{\phi}), \quad Y = Y(\overline{\phi}), \quad T = T(\overline{\phi}), \quad h = h(\overline{\phi}), \tag{2.7}$$

where p, T and the enthalpy $h = e + p/\rho$ are computed from the EOS; likewise, the fluxes are functions of $\overline{\phi}$:

$$\sigma_{ij} = \sigma_{ij}(\overline{\phi}), \quad j_{\alpha j} = j_{\alpha j}(\overline{\phi}), \quad q_{IKj} = q_{IKj}(\overline{\phi}). \tag{2.8}$$

For a Newtonian fluid,

$$\sigma_{ij} = \mu \left(\frac{\partial u_i}{\partial x_j} + \frac{\partial u_j}{\partial x_i} - \frac{2}{3} \frac{\partial u_k}{\partial x_k} \delta_{ij} \right), \quad S_{ij} = \frac{1}{2} \left(\frac{\partial u_i}{\partial x_j} + \frac{\partial u_j}{\partial x_i} \right), \tag{2.9}$$

where μ is the viscosity and S_{ij} is the rate-of-strain tensor.

The molecular species-mass and heat fluxes originate in the fluctuation–dissipation theory (see Keizer 1987), which is consistent with non-equilibrium thermodynamics, converges to kinetic theory in the low-p limit, and relates fluxes and forces from first principles. For a binary-species system (light species 1, heavy species 2), the molecular species-mass and heat fluxes, including Soret and Dufour effects (Harstad & Bellan 2000), are

$$\boldsymbol{j}_2(\overline{\psi}) = B_Y(\overline{\psi}) \nabla Y_2(\overline{\phi}) + B_T(\overline{\psi}) \nabla T(\overline{\phi}) + B_P(\overline{\psi}) \nabla p(\overline{\phi}), \tag{2.10}$$

$$\boldsymbol{q}_{IK}(\overline{\psi}) = C_Y(\overline{\psi}) \nabla Y_2(\overline{\phi}) + C_T(\overline{\psi}) \nabla T(\overline{\phi}) + C_P(\overline{\psi}) \nabla p(\overline{\phi}), \tag{2.11}$$

where $\overline{\psi} \equiv \psi(\overline{\phi})$ and functionally

$$B_Y \equiv -\rho D \alpha_D, \qquad C_Y \equiv -\rho D \alpha_D \alpha_{IK} R_u T \frac{m}{m_1 m_2}, \tag{2.12}$$

$$B_T \equiv -\alpha_{BK} Y_1 Y_2 \frac{\rho D}{T}, \qquad C_T \equiv -\lambda - \rho D \alpha_{IK} \alpha_{BK} R_u \frac{m}{m_1 m_2} Y_1 Y_2, \tag{2.13}$$

$$B_P \equiv -\rho D \frac{Y_1 Y_2}{R_u T} \frac{m_2 m_1}{m} \Lambda, \quad C_P \equiv -\rho D \alpha_{IK} \Lambda Y_1 Y_2. \tag{2.14}$$

In (2.12)–(2.14),

$$\alpha_{BK} = \alpha_{IK} - \alpha_h, \quad \alpha_h = \frac{1}{R_u T} \frac{m_2 m_1}{m} \Theta, \tag{2.15}$$

$$\Lambda \equiv \left(\frac{1}{m_2} \frac{\partial v}{\partial X_2} - \frac{1}{m_1} \frac{\partial v}{\partial X_1} \right), \quad \Theta \equiv \left(\frac{1}{m_2} \frac{\partial (mh)}{\partial X_2} - \frac{1}{m_1} \frac{\partial (mh)}{\partial X_1} \right), \tag{2.16}$$

$$\alpha_D \equiv 1 + X_\alpha \frac{\partial \ln \gamma_\alpha}{\partial X_\beta}, \tag{2.17}$$

where λ is the thermal conductivity with $\lim_{p \to 0} \lambda = \lambda_{KT}$ as discussed in Harstad & Bellan (2000) and the subscript KT denotes the kinetic theory, R_u is the universal

Species	m (g mol^{-1})	T_c (K)	p_c (MPa)
H$_2$	2.016	33.0	1.284
He	4.003	5.19	0.227
O$_2$	31.999	154.6	5.043

TABLE 1. Pure species properties.

gas constant, m is the mixture molar mass, and v is the molar volume with $v = m/\rho$. For species α, m_α is the species-α molar mass, $X_\alpha = mY_\alpha/m_\alpha$, and γ_α is the fugacity. Furthermore, α_{IK} is the IK form of the thermal diffusion factor, α_{BK} is the Bearman–Kirkwood (BK) form of the thermal diffusion factor, D is the binary diffusion coefficient and α_D is the mass diffusion factor.

The models for the unclosed terms in (2.1)–(2.4), namely $\tau_{ij}, \zeta_j, \eta_{\alpha j}$ and $(\nabla \cdot [\overline{q_{IKj}(\phi)} - q_{IKj}(\bar{\phi})])$ are described in §2.4.1 and §2.4.2, respectively.

2.2. *Equation of state*

The pressure is calculated from the well-known PR EOS, given T and the PR molar volume (v_{PR}), as

$$p = \frac{R_u T}{(v_{PR} - b_m)} - \frac{a_m}{(v_{PR}^2 + 2b_m v_{PR} - b_m^2)}, \tag{2.18}$$

where a_m and b_m are functions of T and X_α, the mathematical forms of which are given in detail by Miller, Harstad & Bellan (2001) and Okong'o *et al.* (2002); solvability effects between the two species are inherently included in the EOS. At high p, the v_{PR} value may differ significantly from that of v (Prausnitz *et al.* 1986) and this difference has been taken into account by using a volume shift (Harstad, Miller & Bellan 1997; Okong'o *et al.* 2002) $v_s = v - v_{PR}$ which is calculated from the EOS using the Gibbs energy. All thermodynamic quantities, including $\alpha_D, h, C_p = (\partial h/\partial T)_{p,X}$ and the speed of sound (a_s), are calculated from the EOS using standard thermodynamic relations (Miller *et al.* 2001; Okong'o *et al.* 2002; Okong'o & Bellan 2002a). The implementation of the EOS to calculate p and T from ρ, e and Y_α uses an iterative fit for the OH and OHe mixtures (Okong'o *et al.* 2002; Selle *et al.* 2007). The pure species properties are listed in table 1.

2.3. *Transport coefficients*

The viscosity, the Schmidt number ($Sc = \mu/(\rho \alpha_D D)$) and the Prandtl number ($Pr = \mu C_p/(m\lambda)$) were calculated from high-pressure single-species transport properties using mixing rules, as in Harstad & Bellan (1998). The calculated values were correlated, as summarized in table 2 (see Appendix for the OHe mixture), and these correlations were then used to compute the transport properties μ, D and λ. The relationship between α_{BK} and α_{IK} stated in (2.15) means that either one can be specified, and the other then calculated.

2.4. *Subgrid-scale models*

2.4.1. *SGS-flux models*

Two categories of models are here used for SGS fluxes ($\tau_{ij}, \eta_{\alpha j}, \zeta_j$), namely constant-coefficient models and dynamic-coefficient models (Germano *et al.* 1991). The constant-coefficient SGS models are the gradient (GRC; Clark, Ferziger & Reynolds 1979) and the scale-similarity models (SSC; Bardina, Ferziger & Reynolds 1980); the dynamic-coefficient models are the dynamic Smagorinsky (Smagorinsky 1963, 1993) model (SMD) and a dynamic 'mixed' model (Clark *et al.* 1979; Vreman,

System	O_2/H_2		O_2/He
$\mu = \mu_R (T/T_R)^n$	$n = 0.75$		$n = 0.59$
$Sc \equiv \mu/(\rho \alpha_D D)$	$\begin{bmatrix} (1.334 - 0.668 Y_2 - 0.186 Y_2^2 - 0.268 Y_2^6) \\ \times [1 + (88.6/T)^{1.5}] \end{bmatrix}$	(A 2)	
$Pr \equiv \mu C_p/(m\lambda)$	$1.335/T^{0.1}$	(A 1)	
α_{IK} or α_{BK}	$\alpha_{BK} = 0.2$		$\alpha_{BK} = 0.25$
T range	200–800 K		100–900 K
p range	$\sim$100 atm		$\sim$100 atm

TABLE 2. Transport properties for binary mixtures. $T_R = (T_1 + T_2)/2$, T in Kelvin; α_{BK} from Harstad & Bellan (1998, 2001).

Geurts & Kuerten 1996) combining the Smagorinsky and gradient model (MGRD). The consideration of dynamic modelling stems from the transient, strongly non-uniform aspect of the present flows.

The GRC model, derived from a Taylor-series expansion (Okong'o & Bellan 2004b), is

$$\vartheta_{GR}(\widetilde{\psi}_m, \widetilde{\psi}_n) = C_{GR} \bar{\Delta}^2 \frac{\partial \tilde{\psi}_m}{\partial x_k} \frac{\partial \tilde{\psi}_n}{\partial x_k}. \tag{2.19}$$

(Note that $\vartheta(\tilde{u}_1, \tilde{u}_1) = \tau_{11}$, $\vartheta(\tilde{u}_2, \tilde{u}_2) = \tau_{22}$, $\vartheta(\tilde{u}_3, \tilde{u}_3) = \tau_{33}$.) Theoretically, C_{GR} is proportional to the moments of inertia of the filtering volume; for a cubic top-hat filter $C_{GR} = 1/12$ (Okong'o & Bellan 2004b).

The SSC model, which postulates similarity between the SGS and the small resolved scale, is (Bardina *et al.* 1980)

$$\vartheta_{SS}(\widetilde{\psi}_m, \widetilde{\psi}_n) = C_{SS} \left(\widehat{\widetilde{\psi}_m \widetilde{\psi}_n} - \widehat{\widetilde{\psi}}_m \widehat{\widetilde{\psi}}_n \right), \tag{2.20}$$

where the overhat ($\widehat{}$) denotes (unweighted) filtering at the test-filter level $\widehat{\Delta}$. The specified test filter width is $\widehat{\Delta}/\bar{\Delta} = 2$, being that generally recommended. While scale similarity would imply that $C_{SS} = 1$, it has been shown that the actual value is filter-width dependent (Clark *et al.* 1979; Liu, Meneveau & Katz 1994; Pruett, Sochacki & Adams 2001; Okong'o & Bellan 2004b).

Dynamic modelling (Germano *et al.* 1991) is based on the assumption that the SGS behaviour is akin to that of the small resolved scales. Then, a test filter is introduced, $\widehat{\Delta}$, $\widehat{\Delta} > \bar{\Delta}$, and by double filtering, $\widehat{\widehat{\Delta}}$, a field with scales larger than those of the resolved field is produced. The effective filter width $\widehat{\widehat{\Delta}}$, not actually used for filtering, corresponds to filtering at $\bar{\Delta}$ followed by filtering at $\widehat{\Delta}$, and its value depends on the filter type. Considering the top-hat filter used here for both the grid and test filter, $\widehat{\widehat{\Delta}}$ is optimally approximated by $\widehat{\widehat{\Delta}}^2 = \bar{\Delta}^2 + \widehat{\Delta}^2$ (Vreman, Geurts & Kuerten 1997). The essence of dynamic modelling is to relate the grid-level SGS flux and the test-level SGS flux to the test-level resolved flux. For any quantity φ, such as h, Y_α or u_i, the grid-level and the test-level SGS fluxes associated with the velocity $\tilde{u}_j$ are denoted as $\vartheta_j(\varphi, u_j)$ and $\mathcal{T}_j(\varphi)$, respectively, and defined as

$$\vartheta_j(\varphi, u_j) = \widetilde{\varphi u_j} - \tilde{\varphi}\tilde{u}_j, \tag{2.21}$$

$$\mathcal{T}_j(\varphi) = \widehat{\widetilde{\varphi u_j}} - \hat{\tilde{\varphi}}\hat{\tilde{u}}_j, \tag{2.22}$$

where $\vartheta_j(u_i, u_j) = \tau_{ij}$, $\vartheta_j(Y_V, u_j) = \eta_j$ and $\vartheta_j(h, u_j) = \zeta_j$. The test-level resolved flux, L_j, is computed through the Germano identity (Germano *et al.* 1991). For

compressible flows, L_j takes the form (Moin *et al.* 1991)

$$L_j(\varphi) \equiv \hat{\bar{\rho}}\mathcal{T}_j - \widehat{\bar{\rho}\vartheta}_j = \widehat{\bar{\rho}\hat{\varphi}\tilde{u}}_j - \frac{\widehat{\bar{\rho}\hat{\varphi}}\,\widehat{\bar{\rho}\tilde{u}}_j}{\hat{\bar{\rho}}}, \tag{2.23}$$

where $\hat{\tilde{\psi}} = \widehat{\bar{\rho}\tilde{\psi}}/\hat{\bar{\rho}}$. In the above equation, $\vartheta_j(\varphi, u_j)$ can be modelled using the generic model coefficient, $C(\varphi)$, as

$$\vartheta_j(\varphi, u_j) = C(\varphi)\mu_j(\varphi, \bar{\Delta}), \tag{2.24}$$

where $\mu_j(\varphi, \bar{\Delta})$ is associated with the filter width, $\bar{\Delta}$, and the velocity, $\tilde{u}_j$. Similarly, $\mathcal{T}_j$ can be modelled as $\mu_j(\hat{\varphi}, \hat{\bar{\Delta}})$, associated with $\hat{\bar{\Delta}}$ and the velocity $\hat{\tilde{u}}_j$. If $C(\varphi)$ is assumed constant within the test filter, then, the left-hand side of (2.23) can be calculated in terms of $C(\varphi)$ as

$$L_j(\varphi) = C(\varphi)M_j(\varphi) = C(\varphi)(\hat{\bar{\rho}}\mu_j(\hat{\varphi}) - \widehat{\bar{\rho}\mu_j}(\varphi)). \tag{2.25}$$

The SMD model relies on the gradient-diffusion (eddy-viscosity) concept, and therefore it does not lend itself to computing variances in general. The SGS fluxes in (2.5) are

$$\vartheta_{SM}(\tilde{\psi}_m, \tilde{u}_j) = -C_{SM}\bar{\Delta}^2 S(\bar{\phi}) \frac{1}{2} \frac{\partial \tilde{\psi}_m}{\partial x_j}, \qquad \psi_m \neq u_j, \tag{2.26}$$

with τ_{ij} modelled in trace-free form as

$$\tau_{ij} - \tfrac{1}{3}\tau_{kk}\delta_{ij} = -C_{SM}\bar{\Delta}^2 S(\bar{\phi}) \left[S_{ij}(\bar{\phi}) - \tfrac{1}{3}S_{kk}(\bar{\phi})\delta_{ij} \right], \tag{2.27}$$

where $S^2(\phi) = S_{ij}(\phi)S_{ij}(\phi)$. The YO model (Yoshizawa 1986) for τ_{kk} is

$$\tau_{kk} = C_{YO}\bar{\Delta}^2 S^2(\bar{\phi}). \tag{2.28}$$

Thus, for the SMD model, μ_j has the mathematical form provided in (2.26) excluding the model coefficient; the coefficients are computed according to (2.25), as shown in (2.30).

The MGRD model, chosen here for its focus on gradient computation through the gradient model (reasons explained in §6.2), follows the approach of Vreman *et al.* (1997): the coefficient of the Smagorinsky model is dynamically calculated and that of the gradient model is kept constant at its theoretical value. For the MGRD model, (2.25) becomes

$$L_j(\varphi) = H_j(\varphi) + C(\varphi)M_j(\varphi), \tag{2.29}$$

with $H_j(\varphi) = (\hat{\bar{\rho}}\vartheta_j(\hat{\varphi}) - \widehat{\bar{\rho}\vartheta_j}(\varphi))$, and ϑ_j is computed using the theoretical value $C_{GR} = 1/12$. Following Lilly (1992), we use a least-squares method to minimize the error in computing the coefficient from an overdetermined equation set, which yields the coefficients

$$C_H(\varphi) = \frac{\langle (L_j(\varphi) - H_j(\varphi))M_j(\varphi) \rangle}{\langle M_j(\varphi) M_j(\varphi) \rangle}, \tag{2.30}$$

where, for the present mixing-layer configuration $\langle \cdot \rangle$ denotes averaging over homogeneous (x_1, x_3) planes. The use of dimensional variables in the present formulation necessitates the separate computation of the SGS-model coefficient, which is a scalar, for each type of SGS flux; all computations use (2.30), where repeated indices summation is performed over the relevant SGS-flux terms. With the exception of the stresses for the Smagorinsky model, the simulations are performed with a single-coefficient formulation for each of the SGS fluxes. When using the

Smagorinsky model, two coefficients are computed: one for the diagonal components (τ_{ii}) and one for the off-diagonal components (τ_{ij}, $i \neq j$). When using the gradient model, a single coefficient is computed for all τ_{ij} components. For each ζ_j and η_j, a coefficient is found by summation over the three components of these SGS fluxes. Specifically, the dynamic coefficient values are computed as follows.

(a) For the dynamic SMD model, μ_j is computed from (2.26)–(2.28), and $H_j = 0$.

(b) For the MGRD model, μ_j is computed from (2.26)–(2.28), and ϑ_j in H_j is computed from (2.19) using $C_{GR} = 1/12$.

2.4.2. *Revisiting of the heat-flux term correction model*

To model ($\nabla \cdot [\overline{q_{IKj}(\phi)} - q_{IKj}(\overline{\phi})]$), Selle *et al.* (2007) have used several approximations, none of which was entirely successful. The most tractable approximation was

$$\overline{\boldsymbol{q}_{IK}(\psi)} \simeq \overline{C_T(\psi)}\nabla T(\overline{\phi}) + \overline{C_P(\psi)}\nabla p(\overline{\phi}) + \overline{C_Y(\psi)}\nabla Y_2(\overline{\phi}), \qquad (2.31)$$

where each function $\overline{C_T(\psi)}$, $\overline{C_P(\psi)}$ and $\overline{C_Y(\psi)}$ was modelled following a Taylor-series expansion in conjunction with the assumption that the filter is a projection which leads to only retaining the second-order term. For example,

$$\overline{C_T(\phi)} - C_T(\overline{\phi}) \equiv \frac{1}{2}\left.\frac{\partial^2 C_T}{\partial \phi_m \partial \phi_n}\right|_{\psi=\overline{\psi}} (\overline{\phi_m \phi_n} - \overline{\phi_m}\,\overline{\phi_n}) = \frac{1}{2}\left.\frac{\partial^2 C_T}{\partial \phi_m \partial \phi_n}\right|_{\psi=\overline{\psi}} \vartheta(\phi_m, \phi_n). \quad (2.32)$$

Due to lack of knowledge regarding the transport coefficients' dependence on ψ, the analytical functions $C_T(\phi)$, $C_P(\phi)$ and $C_Y(\phi)$ are typically not available, and thus a numerical multivariate differentiation technique was used to obtain the results. When the DNS-computed $(\overline{C_T(\phi)} - C_T(\overline{\phi}))$, $(\overline{C_P(\phi)} - C_P(\overline{\phi}))$ and $(\overline{C_Y(\phi)} - C_Y(\overline{\phi}))$ were compared in (x_1, x_2) planes to the corresponding model (e.g. that of (2.32) for $(\overline{C_T(\phi)} - C_T(\overline{\phi}))$), the results were very encouraging; however, when these results were used in conjunction with a Taylor expansion of the entire heat flux approximated by (2.31), the DNS-extracted difference $\nabla \cdot (\overline{q_{IKi}(\phi)} - q_{IKi}(\overline{\phi}))$ did not compare well the model predictions, indicating that this approach may not be appropriate. We show in §6.1 that the large gradients in the HDGM regions, which were approximated in Selle *et al.* (2007) using the filtered flow field, e.g. $\overline{\nabla T(\phi)} \simeq \nabla T(\overline{\phi})$, were responsible for the lack of success.

The interest is here in developing a model for each of $\overline{\nabla T(\phi)}$, $\overline{\nabla Y_2(\phi)}$ and $\overline{\nabla p(\phi)}$, as functions of $\nabla T(\overline{\phi})$, $\nabla Y_2(\overline{\phi})$ and $\nabla p(\overline{\phi})$, respectively. We adopt the frame of mind of Carati, Winckelmans & Jeanmart (2001), who partition the range of scales into three distinct regions. Region A is that of the resolved, and thus represented, scales in LES. Region B has the same scale support as region A, but comprises scales smaller than the filter size but larger than, or equal to, the grid scale; these scales are represented and underresolved because although they enter the LES solution and are thus represented, the information for these scales has been filtered. Finally, region C comprises scales smaller than the LES grid, and is thus not represented in LES; this region is portrayed through SGS models in LES. The goal here is to recover the effect of represented and underresolved scales on the resolved scales, and to this end we consider deconvolution methods (e.g. Geurts 1997 who constructed higher-order polynomial inversions). Among deconvolution methods, the focus is here on the approximate deconvolution model (ADM) described in Stolz & Adams 1999, and in Stolz, Adams & Kleiser 2001. The ADM procedure is based on the fact that if spatial filtering is defined through (1.1), then an approximate deconvolution ϕ^* can

be obtained by applying an operator Q_N,

$$\phi^* = Q_N * \overline{\phi}. \tag{2.33}$$

We choose to apply ADM to ϕ rather than ψ because it is ϕ which is computed in DNS, and thus its reconstruction has better accuracy potential than ψ which is calculated from ϕ using for T the strongly nonlinear EOS, as discussed in §2.2. The ADM procedure is based on the assumption that G has an inverse G^{-1}, and in that case the inverse operator is expandable in a series of filter operators. Some filters may not be invertible, but a regularized inverse operator Q_N is obtainable by truncating the series at integer N (Stolz *et al.* 2001), obtaining a regularized approximation of G^{-1},

$$Q_N = \sum_{l=0}^{N} (I - G)^l \approx G^{-1}, \tag{2.34}$$

where regularization is defined as the process through which subgrid-scale dissipation is provided, I is the identity operator and N is the order of the reconstruction. Thus,

$$\phi^* = \left[\sum_{l=0}^{N} (I - G)^l \right] * \overline{\phi}$$
$$= \overline{\phi} + (\overline{\phi} - \overline{\overline{\phi}}) + (\overline{\phi} - 2\overline{\overline{\phi}} + \overline{\overline{\overline{\phi}}}) + \cdots .$$
$$= 3\overline{\phi} - 3\overline{\overline{\phi}} + \overline{\overline{\overline{\phi}}} + \cdots . \tag{2.35}$$

Generally, it has been found (Stolz *et al.* 2001) that $N = 3$ is sufficient to bring an improvement in that $(\phi^* - \overline{\phi})$ is not null, and for $N \geqslant 5$ the value of $(\phi^* - \overline{\phi})$ did not change appreciably from that obtained with $N < 5$. However, it is possible that in other situations than those studied by Stolz *et al.* (2001) there could be another asymptotic best value of N, which will be investigated in §6.1. Noteworthy, the ADM only takes into account the solution obtained at the LES scale and does not involve accurate information at the subgrid scale since that accurate information is unavailable in LES and instead replaced by the SGS – in particular SGS-flux – models. Thus, the result of the ADM is SGS-model dependent.

When considering the heat flux symbolically written as

$$\overline{\boldsymbol{q}_{IK}(\boldsymbol{\phi})} = \sum_{j=1}^{j=3} \overline{C_{A_j}(\phi)\nabla A_j(\phi)}, \tag{2.36}$$

several models for $\overline{\boldsymbol{q}_{IK}(\boldsymbol{\phi})}$ are possible as follows:

$$\overline{\boldsymbol{q}_{IK}(\boldsymbol{\phi})} = \sum_{j=1}^{j=3} C_{A_j}(\overline{\phi})\nabla A_j(\overline{\phi}) \quad \text{No HF}, \tag{2.37}$$

$$\overline{\boldsymbol{q}_{IK}(\boldsymbol{\phi})} = \sum_{j=1}^{j=3} \overline{C_{A_j}(\phi^\star)\, \nabla A_j(\phi^\star)} \quad \text{M1}, \tag{2.38}$$

$$\overline{\boldsymbol{q}_{IK}(\boldsymbol{\phi})} = \sum_{j=1}^{j=3} \overline{C_{A_j}(\phi^\star)}\, \overline{\nabla A_j(\phi^\star)} \quad \text{M2}, \tag{2.39}$$

$$\overline{\boldsymbol{q}_{IK}(\phi)} = \sum_{j=1}^{j=3} \overline{C_{A_j}(\phi^\star)} \ \nabla A_j(\overline{\phi}) \qquad \text{M3,} \qquad (2.40)$$

$$\overline{\boldsymbol{q}_{IK}(\phi)} = \sum_{j=1}^{j=3} C_{A_j}(\overline{\phi}) \ \overline{\nabla A_j(\phi^\star)} \qquad \text{M4,} \qquad (2.41)$$

$$\overline{\boldsymbol{q}_{IK}(\phi)} = \sum_{j=1}^{j=3} \overline{C_{A_j}(\overline{\phi}) \ \nabla A_j(\overline{\phi})} \qquad \text{M5,} \qquad (2.42)$$

where 'HF' is the acronym for the heat flux correction model. The most sophisticated model is M1 where all coefficients and gradients are computed using a reconstructed vector ϕ, ϕ^*, after which the product of each coefficient and associated gradient is filtered and the three contributions according to (2.11) are added. The least sophisticated model is the 'No HF' model case which uses the FC-DNS solution, and the second least sophisticated is M5 which also entirely relies on the filtered flow field. Between M1 and M5 are various approximations where either ϕ^* is used but the filtering is individually performed on coefficients and gradients, or in which either the coefficient of the gradient is computed from $\overline{\phi}$ rather than ϕ^*. Each of these models is investigated in §6.1. Without $\boldsymbol{q}$-correction, in (2.3),

$$(\nabla \cdot \boldsymbol{q}(\phi_{LES}) + (\overline{\nabla \cdot \boldsymbol{q}(\phi)} - \nabla \cdot \boldsymbol{q}(\phi_{LES}))) \ \text{is computed as } \nabla \cdot \boldsymbol{q}(\phi_{LES}). \qquad (2.43)$$

With $\boldsymbol{q}$-correction, in (2.3),

$$(\nabla \cdot \boldsymbol{q}(\phi_{LES}) + (\overline{\nabla \cdot \boldsymbol{q}(\phi)} - \nabla \cdot \boldsymbol{q}(\phi_{LES}))) \ \text{is computed as } \overline{\nabla \cdot \boldsymbol{q}(\phi^*)}. \qquad (2.44)$$

3. Description of the DNS database

The DNS database consists of supercritical temporal mixing-layer simulations ($\mathcal{N} = 2$) of OH or OHe (subscripts o, h and he for oxygen, hydrogen and helium, respectively) mixtures. The temporal configuration is only a surrogate for a spatial mixing layer which is the subject of experiments, and is meant to mimic what would be observed were a vortex, or a small collection of vortices, to be followed downstream. Due to the periodic boundary conditions in two directions, only vortices of a given wavelength or multiples of that wavelength can be simulated. The DNS methodology has been previously described (Miller *et al.* 2001; Okong'o *et al.* 2002; Okong'o & Bellan 2002*a*). The database represents solutions of the differential conservation equations (Miller *et al.* 2001; Okong'o *et al.* 2002; Okong'o & Bellan 2002*a*) and the EOS (see §2.2), utilizing transport coefficient models (see §2.3). These equations were numerically solved using a fourth-order explicit Runge–Kutta time integration in conjunction with a sixth-order compact scheme with eighth-order filter for spatial derivatives (Kennedy & Carpenter 1994); the filtering (applied at interior points only) is required to maintain numerical stability for long-time integrations but since it acts only on the shortest waves that can be resolved on the grid, it does not act as a turbulence model allowing underresolved computations. A parallelization using three-dimensional domain decomposition and message passing, and an efficient parallel tridiagonal solver (Muller & Scheerer 1991) were used.

The configuration is illustrated in figure 1 for the OH case, which shows the mixing layer composed of the two streams (species 1 and 2 initially reside in the

Run	Re_0	$T_2; T_1$	ρ_2/ρ_1	$\lambda_1/\delta_{\omega,0}$	F_{2D}	F_{3D}	$L_1 \times L_2 \times L_3$ (m^3)	Δx (10^{-4} m)	$Re_{m,tr}$	t_{tr}^*
OH750	750	400; 600	24.40	7.29	0.1	0.05	$0.200 \times 0.200 \times 0.120$	5.77	1507	150
OHe600	600	235; 287	12.17	9.31	0.05	0.0125	$0.255 \times 0.255 \times 0.153$	7.36	2004	220

TABLE 3. Listing of the direct numerical simulation realizations and associated resolution. Both simulations were performed at $p_0 = 100$ atm and $M_{c,0} = 0.4$. L_i is the size of the domain in the x_i-direction (in metres). For both layers, $L_1 = 4\lambda_1$ and $\delta_{\omega,0} = 6.859 \times 10^{-3}$ m. For both simulations the grid has $352 \times 352 \times 208$ nodes. The subscript tr denotes the transitional time.
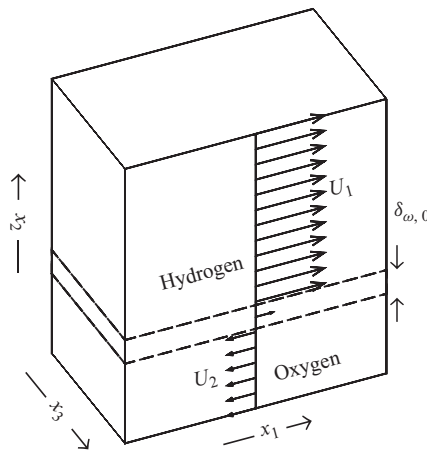
FIGURE 1. O_2/H_2 mixing-layer configuration.

upper and lower streams, respectively), and the streamwise (x_1), cross-stream (x_2) and spanwise (x_3) coordinates. The layer is not symmetric in extent in the x_2-direction, to accommodate the larger layer growth in the lighter fluid side. The free-stream density (ρ_1 or ρ_2) is calculated for each pure species at its free-stream temperature (T_1 or T_2) and at the initial uniform pressure (p_0). The vorticity thickness is defined as $\delta_\omega(t) = \Delta U_0/(\partial\langle u_1\rangle/\partial x_2)_{max}$, where $\Delta U_0 = (U_1 - U_2)$ is the velocity difference across the layer. Here U_1 and U_2 were chosen so as to keep the ultimate vortex stationary in the computational domain (Papamoschou & Roshko 1988; Miller *et al.* 2001); the specification of the convective Mach number (see table 3), $M_{c,0}$, determines ΔU_0. Given the initial streamwise velocity profile u_1 based on U_1 and U_2, $(\partial\langle u_1\rangle/\partial x_2)_{max}$ and hence $\delta_{\omega,0} \equiv \delta_\omega(0)$ are calculated. The initial momentum ratio $|\rho_2 U_2|/|\rho_1 U_1| \sim 5$ for the OH layer and 3.5 for the OHe layer, as the choice of T_2 and T_1 for OHe determines ρ_2 and ρ_1 which together with information from the EOS yields U_1 and U_2. Although the momentum ratio has different values for the two layers, the momentum flux ratio, $(\rho_2 U_2^2/\rho_1 U_1^2)$, is unity for both layers. The specified value of the initial flow Reynolds number, $Re_0 = (1/2)(\rho_1 + \rho_2)\Delta U_0 \delta_{\omega,0}/\mu_R$, chosen so as to enable the resolution of all relevant length scales, is then used to calculate μ_R, which scales μ. The uniform grid spacing is approximately inversely proportional to Re_0, as suggested by the relationship $l/\eta_K \sim Re^{3/4}$ (Tennekes & Lumley 1989), where l is the integral scale and η_K is the Kolmogorov scale.

The simulations were started with error-function profiles for the mean streamwise velocity, mass fraction and temperature, upon which were imposed spanwise and

streamwise vorticity perturbations (similar but not exactly the same as in Moser & Rogers 1991, 1993) of strengths F_{2D} and F_{3D} respectively, whose streamwise (λ_1) and spanwise (λ_3) wavelengths are $\lambda_1 = C\delta_{\omega,0}$ and $\lambda_3 = 0.6\lambda_1$, where $C = 7.29$ is the most unstable wavelength for incompressible flow. For the OHe DNS listed in table 3, the value of C was obtained from a stability analysis (similar to Okong'o & Bellan 2003). Indeed, the study of similarity profiles (Okong'o & Bellan 2003) revealed that to adequately resolve the mean flow would require a resolution that would be an order of magnitude larger in the x_2-direction than feasible in DNS; these similarity profiles differed significantly from that for the incompressible case due to both the equation of state and transport properties. To enable DNS, as an approximation, we used the error function for the mean profile, which is the similarity solution for incompressible flow. The result of using the error function was obtaining large-amplitude p waves at the beginning of the simulation (Okong'o & Bellan 2002a). These waves were let out of the domain with minimal reflection, having imposed in the x_2-direction outflow-type boundary conditions for real gas as derived by Okong'o & Bellan (2002b); the boundary conditions were periodic in the x_1- and x_3-directions. The outflow conditions based on real-gas analysis were indispensable to maintain numerical stability. The flow adjusted to the initial conditions and by the time of roll-up, the pressure waves had left the domain, sweeping out the prevailing u_2. The choice of the error function as the mean profile also influenced the choice of the vorticity perturbations (studied extensively in Okong'o & Bellan 2004c) and the approximation resulted in $\langle u_3 \rangle / \Delta U_0 = O(10^{-3})$ instead of null; in comparison, $\langle u_1 \rangle / \Delta U_0 = O(1)$. The vorticity perturbations resulted in a slight skewing of the free-stream velocities, so that they are no longer aligned, and this does have an effect on the development of the mixing layer. However, animations in (x_1, x_3) planes showed no drift of the layer evolving structures in the x_3-direction.

The grid was the same for both OH and OHe simulations, being chosen to accommodate four wavelengths in the streamwise and spanwise directions, and the layer evolution encompassed roll-up and two pairings of the four initial spanwise vortices into an ultimate vortex.

The DNS database is summarized in table 3, including the transitional time $t_{tr}^* = t_{tr}\Delta U_0/\delta_{\omega,0}$ and the value of the momentum-thickness-based Reynolds number, $Re_m = Re_0\delta_m/\delta_{\omega,0}$, at transition, with

$$\delta_m = \frac{\int_{x_{2,min}}^{x_{2,max}} [\langle \rho u_1 \rangle_{x_2,max} - \langle \rho u_1 \rangle][\langle \rho u_1 \rangle - \langle \rho u_1 \rangle_{x_2,min}]\mathrm{d}x_2}{(\langle \rho u_1 \rangle_{x_2,max} - \langle \rho u_1 \rangle_{x_2,min})^2}, \tag{3.1}$$

where $x_{2,max} = L_2/2$, $x_{2,min} = -L_2/2$ (Okong'o & Bellan 2002a), and t_{tr} is the time at which the one-dimensional velocity-fluctuation-based energy spectra become smooth (indicating the achievement of a continuum of scales typical of turbulence), except for the forcing frequency. For each DNS, the transitional state, which is the one analysed *a priori* by Selle *et al.* (2007) and *a posteriori* here, exhibited some persistent coherent structures and in this sense this state was not akin to a self-similar state of a temporal mixing layer. As shown in Selle *et al.* (2007), the transitional state displayed the salient characteristics experimentally observed in supercritical fully turbulent flows that are the HDGM regions. The combination of these salient characteristics and smooth spectra made these transitional states relevant for assessing SGS models for supercritical turbulent flows. The goal of the LES is to reproduce the dependent variables, e.g. mean values, fluctuations and as much as possible their

spatial distribution exhibited by the HDGM regions. The HDGM regions, discussed by Miller *et al.* (2001) and Bellan (2006), redistribute turbulent energy from the normal direction to the tangential direction, as found in the experiments of Hannoun, Fernando & List (1988) at sharp density boundaries. Unless one can capture this local aspect of the flow, it is very unlikely that phenomena crucial to mixing and combustion could be accurately predicted in propulsion systems; particularly, the p-distribution has a strong impact on the prediction of the velocity field and the T, Y and p gradients influence the heat flux computation (see (2.11)).

4. LES initial and boundary conditions

Consistent with the LES equations, which are obtained from the original conservation equations through filtering, the LES initial conditions are also obtained by filtering followed by grid coarsening (e.g. Vreman *et al.* 1997; Geurts & Frohlich 2002; Leboissetier, Okong'o & Bellan 2005) to retain only those nodes that will be used in LES.

The boundary conditions are periodic in the x_1 and x_3 homogeneous directions and non-reflective in the x_2-direction, similar to that of DNS. The non-reflective boundary conditions, which were developed on the equivalent Euler equations (Okong'o & Bellan 2002*b*), do not explicitly involve the q-correction term. In these boundary conditions, the dependent variables are those computed in LES, which, according to the SGS model, may or may not contain the q-correction term.

5. LES numerical methodology

The numerical method in LES is essentially the same as in DNS (see §3), so as to attribute differences between LES and DNS to the SGS models rather than the numerical method. For LES to be meaningful, the computational grid must be specified to be fine enough to represent the mean initial profiles and to resolve the large eddies, and coarse enough to require SGS modelling.

The chosen grid for LES is here $\Delta x_{LES} = 4\Delta x_{DNS}$. This grid resolution is justified by the energy spectra and also by LES comparisons both with FC-DNS and an LES devoid of SGS-flux model, called the 'No SGS' model case; see §6.2. Although the mathematical form of the equations for the combined No SGS model with the No HF model is identical to the unfiltered equations, the meaning of the dependent variables is different since in the first case the computed solution is that of the filtered equations; the meaning of the variables is important when one wishes to compare simulation results with experimental data. Thus, even for the No SGS model with No HF model case, the scientific target is to reproduce the FC-DNS. Because of the identical form of the equations, one may consider the No SGS model with No HF model case to be an underresolved DNS, depending on the viewpoint of interest, and then it should be compared to the coarsened DNS. A coarser LES grid than $\Delta x_{LES} = 4\Delta x_{DNS}$ cannot resolve the initial shear layer well enough to credibly represent in LES the initial conditions of the DNS study.

The grid and test filters have a cubic top-hat mathematical form (for which the filtered value is simply the integrated value over the filter width), being the only one consistent with easy interpretation of results when using a finite difference scheme. The spatial discretization is the same sixth-order accurate compact scheme used in the DNS, and time integration is also performed using a fourth-order explicit Runge–Kutta scheme, as in DNS. The $\bar{\Delta}$ width is a compromise between retaining

the maximum amount of information in the resolved scales and minimizing the discretization-error influences. In order to limit numerical errors, $\bar{\Delta}/\Delta x_{LES}$ must be chosen according to the accuracy of the space discretization scheme, irrespective of the grid resolution. For a sixth-order Padé scheme, this ratio must be $\bar{\Delta}/\Delta x_{LES} \geqslant 2$ (Ghosal 1996; Chow & Moin 2003), and the present choice is $\bar{\Delta} = 2\Delta x_{LES}$, meaning that the smallest resolved eddy is represented by at least two grid points.

Time stability is ensured by applying an explicit high-order filter to the conservative variables in each spatial direction. Since the role of this filter is to prevent aliasing from contaminating the lower wavenumber scales of the solution (Kennedy & Carpenter 1994), it is sometimes advisable to filter at every time step. Although for the well-resolved DNS grid the frequency of the high-order filtering is not expected to alter the solution, for LES devoid of an SGS model, since the LES grid resolution is only sufficient to resolve the large scales, the selected filtering frequency is expected to affect the solution. After some experimentation, we filtered the solution every five time steps for all LES, including those devoid of SGS models (i.e. either No HF or No SGS models). Additionally, unlike in DNS where filtering is not performed at the domain boundaries, here filtering is performed over the entire domain including the points at and near the non-periodic boundaries, and the order of the filter is increased from eight as used in DNS, to twelve in the interior, with sixth-order boundary closures. Finally, the CFL number was unity, as in the DNS.

6. Results

The solution of the LES (2.1)–(2.4) and (2.18), ϕ_{LES}, and the equivalent $\psi_{LES} \equiv \psi(\phi_{LES})$, are each here compared to the solution represented by $\bar{\phi}$ computed from the FC-DNS and the corresponding vector $\overline{\psi} = \psi(\bar{\phi})$. As stated in § 1, ϕ_{LES} will be here compared to $\bar{\phi}$ at the LES grid nodes and the hope when using the *q*-correction model in conjunction with an SGS-flux model is to obtain a ϕ_{LES} that is closer to $\bar{\phi}$ than when using an SGS-flux model alone, so as to enhance the prediction accuracy when utilizing coarse grids. We first revisit our previous *a priori* study (Selle *et al.* 2007) in § 6.1 by examining the performance of the heat-flux correction models proposed in § 2.4.2. Then, we select the best *q*-correction term model and in § 6.2 we assess, *a posteriori*, LES results obtained either without or with the *q*-correction in conjunction with a variety of SGS-flux models for OH750; for OHe600 LES we only use a selection of the SGS-flux models utilized for OH750. The stringent goal here is to reproduce in LES both the spatial and temporal equivalence of the FC-DNS. If only statistical equivalence is desired (Pope 2004), the flexibility in the choice of a model is considerably larger.

6.1. *Revisiting the* a priori *study on the heat-flux correction*

Unlike in Selle *et al.* (2007), we rank here the magnitude of terms in the LES energy equation based on x_2-r.m.s. activity using the FC-DNS, and as in Selle *et al.* (2007) we use this information to assess the need for a molecular SGS model (the *q*-correction) additional to a model for the typical SGS heat flux. Having established that such additional SGS models are needed, models No HF and M1–M5 are then evaluated to understand their capabilities in reproducing the desired term; as stated in § 2.4.2, the goal is to obtain a model which minimizes $(\nabla \cdot [\overline{q_{IKj}(\phi)} - \overline{q_{IKj}(\phi)}_M])$, where the subscript M denotes a model. We next examine the influence of the N value and finally we inspect the impact of the filter discrete representation on the accuracy of the model.

Energy	$t^* = 25$	$t^* = 50$	$t^* = 100$	$t^* = 150$
$\dfrac{\partial}{\partial x_j}(\bar{\rho}\tilde{e}_t\tilde{u}_j)$	52.39	123.67	191.59	199.63
$\dfrac{\partial}{\partial x_j}[p(\bar{\phi})\tilde{u}_j]$	21.09	50.08	78.11	81.56
$\dfrac{\partial}{\partial x_j}(\bar{\rho}\zeta_j)$	17.17	40.80	40.10	32.22
$\dfrac{\partial}{\partial x_j}[q_{IKj}(\bar{\phi})]$	11.51	21.07	28.40	25.27
$\dfrac{\partial}{\partial x_j}[\Delta(\bar{q}_{IKj})]$	5.70	11.77	11.92	8.15
$\dfrac{\partial}{\partial x_j}(\bar{\rho}\tau_{ij}\tilde{u}_i)$	0.36	0.82	0.82	0.65
$\dfrac{\partial}{\partial x_j}[\sigma_{ij}(\bar{\phi})\tilde{u}_i]$	0.49	0.65	0.78	0.52
$\dfrac{\partial}{\partial x_j}[\Delta(\overline{\sigma_{ij}u_i})]$	0.23	0.33	0.31	0.18
$\dfrac{\partial}{\partial x_j}\{\Delta(\bar{p})\tilde{u}_j\}$	0.11	0.23	0.21	0.16
$\dfrac{\partial}{\partial x_j}(\bar{\rho}\kappa_j - \bar{\rho}\tau_{ij}\tilde{u}_i)$	0.15	0.31	0.21	0.14

$$\Delta(\bar{f}) \equiv \overline{f(\phi)} - f(\bar{\phi})$$

TABLE 4. Magnitude (x_2 r.m.s.) of terms in LES equations at $t^* = 25$, 50, 100 and 150. The computation is performed using the O_2/H_2 DNS database for $\bar{\Delta} = 8\Delta x$. Units are 10^9 J m^{-3} s^{-1}.

#### 6.1.1. x_2-r.m.s. activity

The r.m.s. activity of each term in the energy equation is computed by integrating its x_2-variation of the homogeneous plane average. The integration is performed at selected times in the layer's development and is tabulated in table 4 for OH and table 5 for OHe. For OH, the table lists the terms ranked from that having the most significant contribution at $t_{tr}^* = 150$ to that with the least contribution at that time station, and for OHe the ranking follows that at $t_{tr}^* = 220$. At all listed times, the leading-order terms are the advection, pressure work, SGS-flux term, molecular heat flux and $\boldsymbol{q}$-correction. Compared to the pressure work which ranks second in order of magnitude, the $\boldsymbol{q}$-correction term varies from 10 % to 27 % of the pressure work magnitude for OH and from 4 % to 8 % for OHe, and thus the impact of the $\boldsymbol{q}$-correction on the total energy prediction is expected to be small. However, at the listed times, the $\boldsymbol{q}$-correction term represents from a minimum of 32 % at $t^* = 150$ to a maximum of 56 % at $t^* = 50$ of the heat flux for the OH case, and the equivalent values for OHe are 35 % at $t^* = 220$ and 64 % at $t^* = 50$. The indication is that the $\boldsymbol{q}$-correction may play an important role in the accurate $\boldsymbol{q}$ prediction.

To complement the tabulated data, the x_2-r.m.s. of the leading-order terms in the LES energy equation are compared using the FC-DNS database and the results are plotted in figure 2 at $t^* = 50$ and $t^* = 150$ for the OH750 layer, and figure 3 at $t^* = 100$ and $t^* = 220$ for the OHe600 layer. For the OHe600 layer, the influence of the $\bar{\Delta}/\Delta x_{DNS}$ ratio is also illustrated. For the OH750 case displayed in figure 2, the advection term has the largest contribution, being followed by the pressure work and

Energy	$t^* = 50$	$t^* = 100$	$t^* = 150$	$t^* = 220$
$\dfrac{\partial}{\partial x_j}(\bar{\rho}\tilde{e}_t\tilde{u}_j)$	36.51	85.03	97.31	136.62
$\dfrac{\partial}{\partial x_j}[p(\bar{\phi})\tilde{u}_j]$	21.44	51.29	56.48	77.40
$\dfrac{\partial}{\partial x_j}(\bar{\rho}\zeta_j)$	13.39	29.25	23.62	24.41
$\dfrac{\partial}{\partial x_j}[q_{IKj}(\bar{\phi})]$	2.64	7.02	7.27	8.17
$\dfrac{\partial}{\partial x_j}[\Delta(\bar{q}_{IKj})]$	1.69	3.78	3.43	2.84
$\dfrac{\partial}{\partial x_j}(\bar{\rho}\tau_{ij}\tilde{u}_i)$	0.52	1.16	1.02	1.43
$\dfrac{\partial}{\partial x_j}\{\Delta(\bar{p})\tilde{u}_j\}$	0.25	0.58	0.56	0.68
$\dfrac{\partial}{\partial x_j}(\bar{\rho}\kappa_j - \overline{\rho\tau_{ij}\tilde{u}_i})$	0.18	0.41	0.29	0.45
$\dfrac{\partial}{\partial x_j}[\sigma_{ij}(\bar{\phi})\tilde{u}_i]$	0.15	0.35	0.36	0.36
$\dfrac{\partial}{\partial x_j}[\Delta(\overline{\sigma_{ij}u_i})]$	0.10	0.19	0.16	0.14

$$\Delta(\bar{f}) \equiv \overline{f(\phi)} - f(\bar{\phi})$$

TABLE 5. Magnitude (x_2 r.m.s.) of terms in LES equations at $t^* = 50$, 100, 150 and 220. The computation is performed using the O_2/He DNS database for $\bar{\Delta} = 8\Delta x$. Units are 10^9 J m^{-3} s^{-1}.
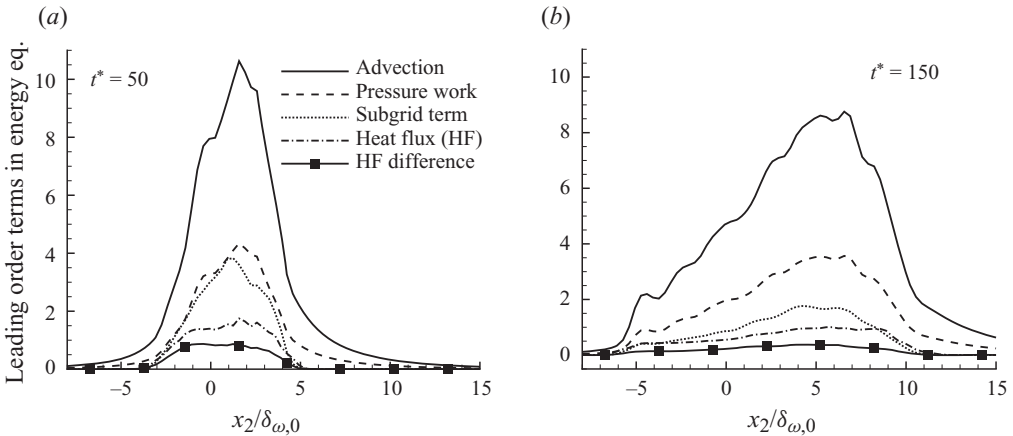
FIGURE 2. The x_2 r.m.s. of the leading-order terms in the energy equation at (a) $t^* = 50$ and (b) $t^* = 150$. The computation is performed using the O_2/H$_2$ DNS with $\bar{\Delta} = 8\Delta x_{DNS}$. HF denotes the heat flux. The values shown are non-dimensionalized by 7×10^{10} J m^{-3} s^{-1}.

the typical SGS-flux (denoted as subgrid in the legend) term, which compete at the early times of the simulation with the pressure work and becomes dominant at $t^* = 100$ (not shown) and $t^* = 150$. The molecular heat flux contribution is approximately half of that of the SGS-flux subgrid term, and that from ($\nabla \cdot [\overline{q(\phi)} - q(\bar{\phi})]$) is half of the
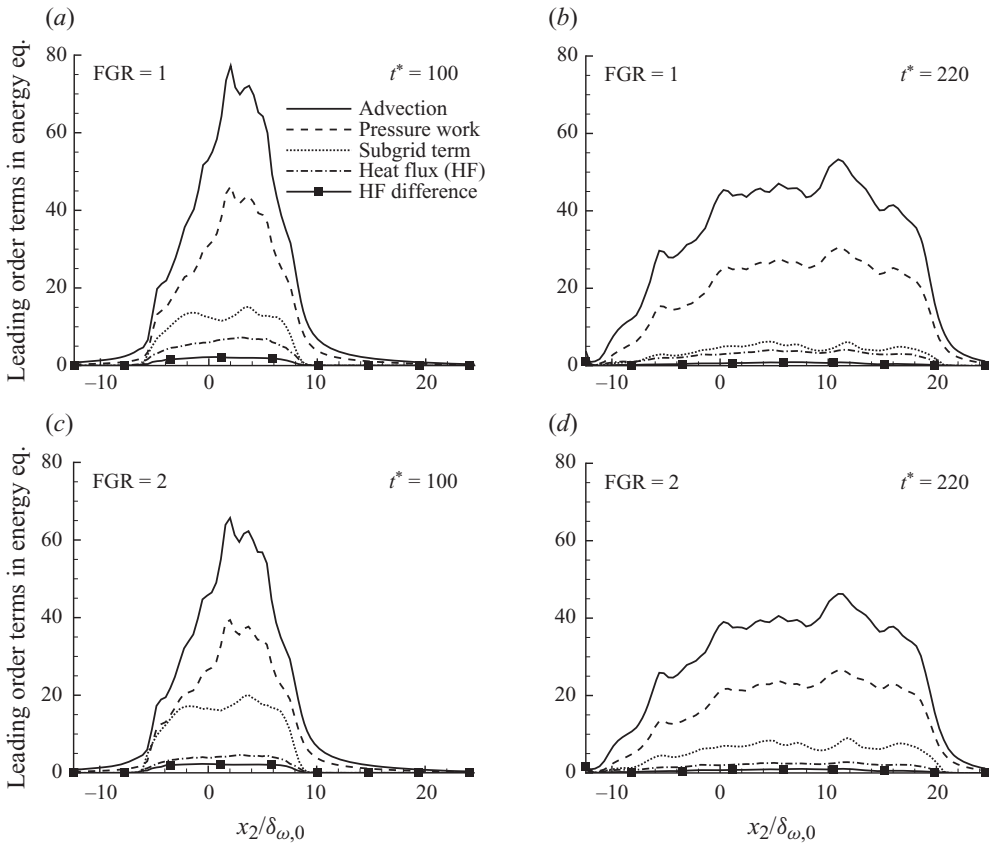
FIGURE 3. The x_2 r.m.s. activity of the leading-order terms in the energy equation for the O$_2$/He DNS database at (*a*, *b*) $\bar{\Delta}/\Delta x_{LES} = 1$ and (*c*, *d*) $\bar{\Delta}/\Delta x_{LES} = 2$ for (*a*, *c*) $t^* = 100$ and (*b*, *d*) $t^* = 220$, where the prospective LES grid size is $\Delta x_{LES} = 4\Delta x_{DNS}$. The values shown are non-dimensionalized by 0.5×10^{10} J m^{-3} s^{-1}.

$\nabla \cdot \mathbf{q}(\overline{\phi})$ value. All other terms in the energy equation are small in comparison, and thus not shown. Based on this analysis we conclude that the $\mathbf{q}$-correction is necessary particularly at the early stages of the layer development and that its contribution is larger than the viscous work term but smaller than the SGS-flux term. The OHe results shown in figure 3 support the conclusions from the OH750 analysis and additionally show that, as expected, when $\bar{\Delta}/\Delta x_{DNS}$ increases, the value of $(\nabla \cdot [\overline{\mathbf{q}(\phi)} - \mathbf{q}(\overline{\phi})])$ increases as well: for $\bar{\Delta}/\Delta x_{DNS} = 4$, the contribution of $(\nabla \cdot [\overline{\mathbf{q}(\phi)} - \mathbf{q}(\overline{\phi})])$ is up to 30 % of $\nabla \cdot \mathbf{q}(\overline{\phi})$ at $t^* = 100$ and up to 25 % at $t^* = 220$, whereas for $\bar{\Delta}/\Delta x_{DNS} = 8$, the corresponding values are approximately 50 % and 40 %, respectively. Thus, if the LES prediction of the effective heat flux is of concern, as it is in liquid rocket engines (Tucker *et al.* 2008), it is apparent that a $\mathbf{q}$-correction term will be necessary in the energy equation.

   To gain a better understanding of the primary effect governing the heat flux in the present DNS, the three terms of (2.11) are further examined for the OH750 layer. The x_2-r.m.s. difference between the filtered heat flux divergence and the heat flux divergence calculated using $\overline{\phi}$ for each of the three terms is compared in figure 4 at $t^* = 50$ and 150. At both t^* values, the maximum contribution is from the species mass-fraction gradient term, being comparable to the heat flux value. The temperature
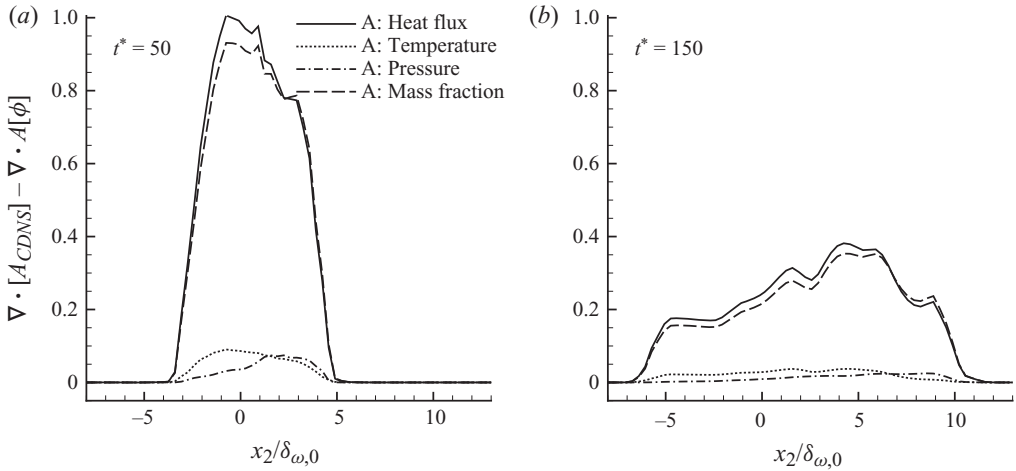
FIGURE 4. The x_2 r.m.s. of the difference for the heat flux and each of its contributions at (a) $t^* = 50$ and (b) $t^* = 150$. The computation is performed using the O_2/H_2 DNS with $\bar{\Delta} = 8\Delta x_{DNS}$. The filtering operation is denoted by square brackets. The values shown are non-dimensionalized by 1.15×10^8 J m^{-3} s^{-1}.

gradient and pressure gradient terms are comparable, being less than one fifth the value of the species mass gradient term. When the difference between the free-stream temperatures is larger than 200 K of the OH750 case, the ratios of the respective contributions may change; indeed, for rocket propulsion applications, this difference will be one order of magnitude larger.

Furthermore, to assess whether $C_{A_j}(\phi)$ or $\nabla A_j(\phi)$ dominate each contribution, the corresponding coefficients and gradients are separately examined using the FC-DNS for the OH750 layer. The species mass-fraction gradient is the smallest but its associated coefficient is the largest among all three coefficients (not shown). The largest difference between the filtered contribution and the contribution computed using the filtered flow field is obtained from the pressure gradient term but since its coefficient is very small, the overall contribution to the heat flux difference due to the pressure gradient is small compared to that of the species mass-fraction gradient term. Based on the high coefficient values of the species mass-fraction gradient contribution (the main contributor of the heat flux; see figure 4), it is natural to hypothesize that the modelling effort should focus on the coefficients; this strategy was the approach of Selle *et al.* (2007). Although Selle *et al.* (2007) were successful in modelling the coefficients, the heat flux representation was deemed unsatisfactory. To investigate this paradox, we examine here both the mean and the r.m.s. of the difference between the filtered term and the term computed using the filtered flow field due to the species mass gradient; the examination is both from the standpoint of coefficients and total contribution to the q-correction. Figure 5(a) illustrates the x_2-r.m.s. of the differences in coefficients, gradients and heat flux at $t^* = 150$. The results show that although the difference between coefficient values is high compared to that between the gradients, there is no correlation between the x_2-distribution of the coefficients' difference and the heat flux difference, whereas the difference in gradients closely follows that of the corresponding term in the heat flux. This indicates that the heat flux difference is governed by the gradients rather than the coefficients. Unrigorously assuming that

$$\overline{C_A(\phi)\nabla A(\phi)} = \overline{C_A(\phi)}\ \overline{\nabla A(\phi)}, \qquad (6.1)$$
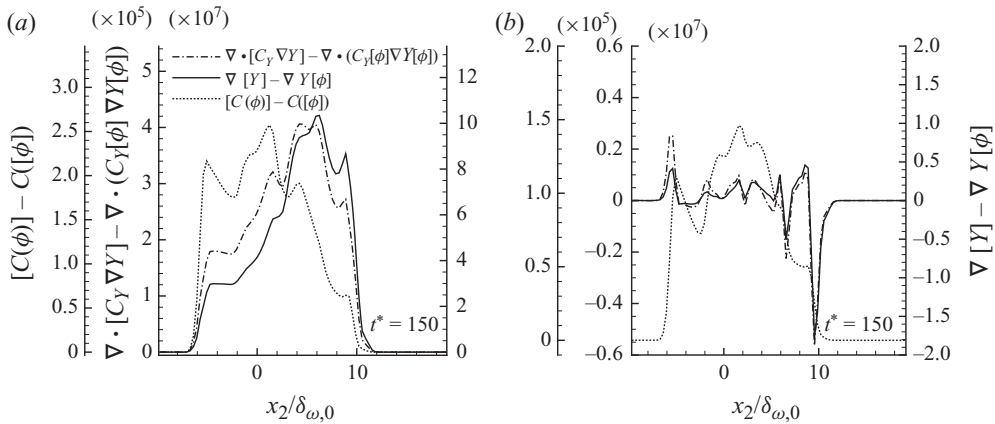
FIGURE 5. Comparison of the difference in coefficients, gradients and the heat fluxes: (*a*) r.m.s and (*b*) mean at $t_{tr}^* = 150$. The computation is performed using the O_2/H_2 DNS with $\bar{\Delta} = 8\Delta x_{DNS}$. The filtering operation is denoted by square brackets. Units are consistent with the heat flux being in J m^{-2} s^{-1}.

then the heat flux difference, proportional to the difference in gradients, becomes

$$\overline{C_A}\,\overline{\nabla A} - C_A(\bar{\phi})\,\nabla A(\bar{\phi}) \simeq \alpha(\overline{\nabla A} - \nabla A(\bar{\phi})). \tag{6.2}$$

This implies that

$$\overline{C_A} \simeq C_A(\bar{\phi}) \simeq \alpha, \tag{6.3}$$

where α is approximately constant. Although having an approximately constant coefficient value seems inconsistent with the aforementioned large difference in species mass coefficients (see figure 5), this seemingly inconsistent result is understood if the coefficient value is examined. Indeed, $(\overline{C_A} - C_A(\bar{\phi}))$ is only 2 % of either of the coefficient's values; hence, it can be considered negligible. This finding highlights why the models proposed in the previous *a priori* study Selle *et al.* (2007), focussing on the coefficient correction rather than the gradient terms, had limited success.

6.1.2. *Effect of the mathematical model*

To measure the effectiveness of *q*-correction (2.37)–(2.42) models, the x_2-r.m.s. activity study of §6.1.1 is now performed for No HF and M1–M5 and the results are listed in table 6 for $N = 2$. As clearly seen from table 6, the minimum difference, $(\partial/\partial x_j)(\overline{q_j(\phi)} - q_j(\phi^*))$, is obtained when using M1, followed by M2 and M4, as expected. These three models are approximately 30 % better than the No HF case. Model M3 is the least satisfactory, yielding results no better than the No HF model, which confirms the importance of the gradient reconstruction rather than that of the coefficients. The main deficiency of the No HF model is the calculation of gradients from $\bar{\phi}$, as in M3. This can be partially avoided if the gradients are calculated from the approximated values instead, ϕ^*, as in M1, M2 and M4. The fact that models M2 and M4, which only differ in calculation of the coefficients, give similar results shows that different coefficient calculations have a small effect on the final outcome, confirming the conclusions of §6.1.1, as also supported by the M3 and No HF model results.

The evaluation of the models' performance is also conducted through a visual inspection of the x_2-r.m.s. activity for models M1–M5 using $N = 5$. Figure 6 displays the difference between the filtered heat flux divergence and the heat flux divergence

		$t^* = 25$	$t^* = 50$	$t^* = 100$	$t^* = 150$
No HF	$\dfrac{\partial}{\partial x_j}(\overline{q_j(\phi)} - q_j(\bar{\phi}))$	5.70	11.77	11.92	8.15
M1	$\dfrac{\partial}{\partial x_j}(\overline{q_j(\phi)} - \overline{q_j(\phi^*)})$	1.60	4.01	3.22	1.46
M2	$\dfrac{\partial}{\partial x_j}(\overline{q_j(\phi)} - \overline{q_j(\phi^*)})$	2.67	5.89	4.78	2.09
M3	$\dfrac{\partial}{\partial x_j}(\overline{q_j(\phi)} - \overline{q_j(\phi^*)})$	5.38	11.17	11.39	7.81
M4	$\dfrac{\partial}{\partial x_j}(\overline{q_j(\phi)} - \overline{q_j(\phi^*)})$	3.19	6.83	5.55	2.38
M5	$\dfrac{\partial}{\partial x_j}(\overline{q_j(\phi)} - \overline{q_j(\bar{\phi})})$	3.93	8.80	10.48	8.74

TABLE 6. Comparison through the x_2-r.m.s. of the modelled filtered heat flux term obtained with the model approximations in (2.38)–(2.42) at $t^* = 25$, 50, 100 and 150 using (2.35). The computation is performed using the O_2/H_2 DNS with $\bar{\Delta} = 8\Delta x_{DNS}$. Units are 10^9 J m^{-3} s^{-1}.
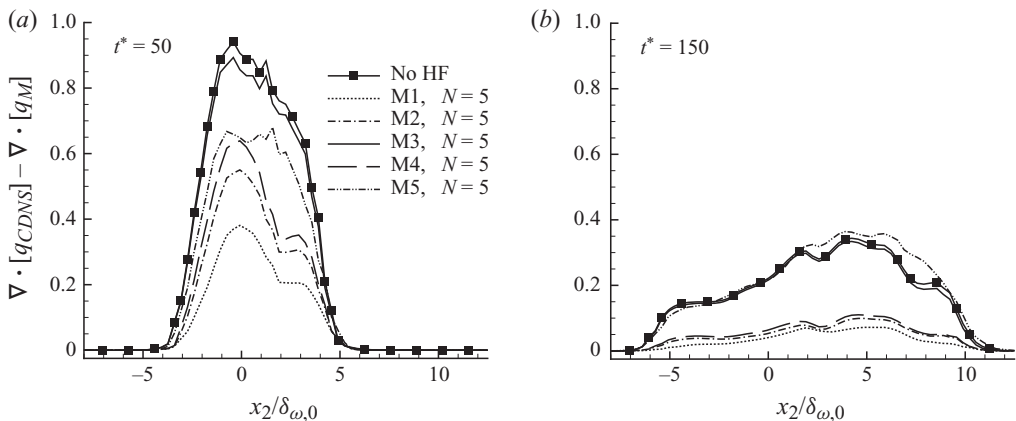
FIGURE 6. The x_2 r.m.s. of the difference between the divergence of the filtered heat flux computed using the O_2/H_2 DNS with $\bar{\Delta} = 8\Delta x_{DNS}$, and the heat flux divergence obtained with the No HF model and M1–M5 reconstruction models (see (2.38)–(2.42)). Results are shown at (a) $t^* = 50$ and (b) $t^* = 150$. The values shown are non-dimensionalized by 6.5×10^{10} J m^{-3} s^{-1}. The filtering operation is denoted by square brackets.

calculated from the filtered field at $t^* = 50$ and 150. The results are consistent with the domain-r.m.s. activity study; the best model is M1, followed by M2; M3 yields comparable results with the No HF model case; M4 produces similar results with M2. The explicit-filtering model (M5) has a better performance than the No HF model at $t^* = 50$, but not at $t^* = 150$.

6.1.3. *Influence of the ADM reconstruction order*

Stolz *et al.* (2001) report that generally $N = 3$ gives acceptable approximations and $N > 5$ does not lead to substantial improvement in the reconstruction. To investigate the effect of the N value for the present purposes, the M1 approximation is obtained using $N \in [0,5]$. For $N = 0$ one recovers M5. The results are displayed in figure 7. As expected, as N increases, the discrepancy between the filtered heat flux and that
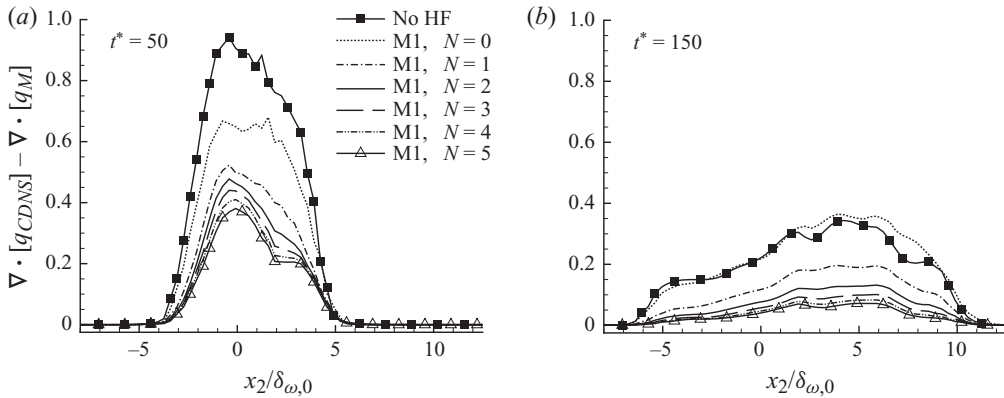
FIGURE 7. Effect of order of reconstruction (r.m.s. activity), N, on the heat flux correction at (*a*) $t^* = 50$ and (*b*) $t^* = 150$. The computations were performed using the O_2/H_2 DNS with $\bar{\Delta} = 8\Delta x_{DNS}$. The values shown are non-dimensionalized by 6.5×10^{10} J m^{-3} s^{-1}. The filtering operation is denoted by square brackets.

computed from the filtered solution decreases. However, consistent with the results of Stolz *et al.* (2001), the improvement after $N = 3$ is minimal. Based on this analysis, we use $N = 3$ as the reconstruction order.

6.1.4. *Impact of the discrete representation of the filter*

Stolz *et al.* (2001) performed ADM using a discrete implicit Padé filter which is different from the top-hat filter (in conjunction with the trapezoidal rule) used in our study. It is thus legitimate to enquire if there is an effect of the discrete representation for the top-hat filter on the reconstruction achieved through ADM. We thus investigate the explicit filter of Stolz *et al.* (2001) along with three other filter formulations.

(i) Filter A. $G(\omega) = (1 + \cos(\omega))/2$, top hat using trapezoidal rule.
(ii) Filter B. $G(\omega) = (2 + \cos(\omega))/3$, top hat using Simpson's rule.
(iii) Filter C. $G(\omega) = (10 + 8\cos(\omega) - 2\cos(2\omega))/16$, explicit Padé filter.
(iv) Filter D. $G(\omega) = (16 - 2\cos(3\omega) + 18\cos(\omega))/32$, explicit filter.

For these filters the transfer functions are shown in figure 8 and the filter-to-grid ratio is 2, except for the explicit Padé filter for which it is 1.5.

Figure 9 displays the r.m.s. of the difference between the divergence of the filtered heat flux and that obtained from the model, i.e. $(\nabla \cdot (\overline{\boldsymbol{q}(\phi)} - \overline{\boldsymbol{q}(\phi)_M}))$, where $\boldsymbol{q}(\phi)$ is calculated on the coarse grid $4\Delta x_{DNS}$. For the No HF model case, $\overline{\boldsymbol{q}(\phi)_M} = \boldsymbol{q}(\bar{\phi})$, which is computed using the FC-DNS. The comparison is between the No HF model at $t^* = 50$ or 150 and the equivalent quantity obtained from M1 using $N = 5$. In figure 9(*a*), the largest and smallest deficits are obtained with Filters D and B, respectively. Considering that Filter B is not as dissipative as the others (see figure 8), obtaining the smallest error when using this filter is not surprising. When M1 is employed, more than half of the discrepancy in heat flux divergence is avoided for all filters. A similar trend is observed at $t^* = 150$; however, the need for $\boldsymbol{q}$-correction is reduced at $t^* = 150$ compared to $t^* = 50$ (see figure 9*b*).

Filter A was adopted in the *a posteriori* study, in concert with our previous LES of supercritical pressure flows (Taşkinoğlu & Bellan 2010).
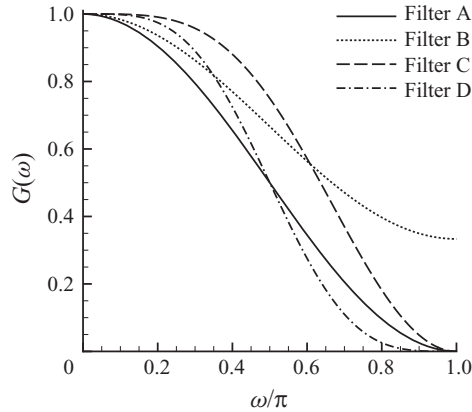
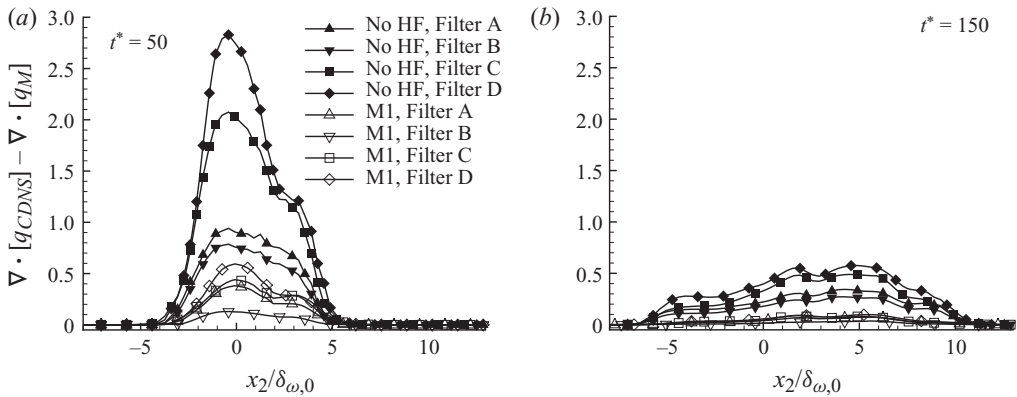FIGURE 8. Transfer functions of the tested filters for which definitions are given in §6.1.4.

FIGURE 9. The x_2 r.m.s. of the difference for the heat flux divergence at (*a*) $t^* = 50$ and (*b*) $t^* = 150$. The computations were performed using the O_2/H_2 DNS with $\bar{\Delta} = 8\Delta x_{DNS}$. The values shown are non-dimensionalized by 6.5×10^{10} J m^{-3} s^{-1}. The filtering operation is denoted by square brackets.

6.2. A posteriori *analysis*

The *a priori* study indicates the need for a *q*-correction term in the energy equation, but the ultimate test for the correction necessity is whether it does improve the LES solution so that it compares more favourably with the FC-DNS. That is, as stated in §1, the desire is to rely on the *q*-correction to reintroduce some of the filtered physics back into LES. Here, we assess whether the *q*-correction can indeed introduce filtered information into LES additional to that introduced by the typical SGS-flux models. The assessment is for the two DNS which were performed for different species mixtures, free-stream temperatures and initial layer perturbations, but that, however, have the same initial momentum flux ratio value of unity. Examination of the *q*-correction model for different species mixtures introduces generality to the concept since both the EOSs and transport properties are species-mixture dependent.

We first examine the effect of the *q*-correction model directly on the heat flux taking as an example the OH750 simulation, and then we continue with an analysis of the dependent variables from the standpoint of x_2-r.m.s. mean values, fluctuations and second-order correlations for the OH750 simulation and spatial visualizations for the OHe600 simulation.
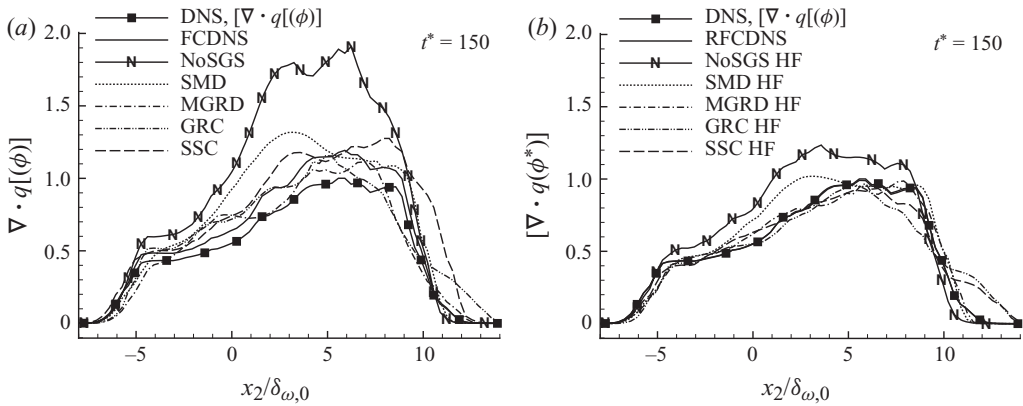
FIGURE 10. The x_2-r.m.s. of several quantities. (*a*) The divergence of the heat flux computed from the filtered flow field of either LES or FC-FNS; the LES is without heat flux correction. (*b*) The filtered divergence of the heat flux computed from the reconstructed flow field of either LES or FC-DNS; the LES is with heat flux correction. The LES with heat flux correction is denoted by HF and is obtained using model M1. The LES use various SGS-flux models, all defined in §2.4.1. All results are displayed at $t_{tr}^* = 150$. The computations were performed using the O_2/H_2 DNS with $\bar{\Delta} = 8\Delta x_{DNS}$. The values shown are non-dimensionalized by 6.5×10^{10} J m^{-3} s^{-1}. The filtering operation is denoted by square brackets.

6.2.1. *Effect of* q-*correction on heat flux computation*

The SGS-flux models used are GRC, SSC, SMD, and the mixed model MGRD. The GRC and SSC models are used with their calibrated coefficient values for $\bar{\Delta}/\Delta x_{DNS} = 8$ obtained from the corresponding DNS at $t_{tr}^* = 150$, as follows:

$$C_{GR} = 0.0910 \qquad\qquad \text{GRC}, \qquad\qquad (6.4)$$

$$C_{SS} = 0.4009 \text{ for } \widehat{\bar{\Delta}} = 2\bar{\Delta} \qquad\qquad \text{SSC}. \qquad\qquad (6.5)$$

As stated in §2.4.1, among all possible dynamic mixed SGS-flux models, MGRD is here selected based on the formulation of the GR model emphasizing the reconstruction of a variable through its gradients (Okong'o & Bellan 2004*b*), which as highlighted in §6.1, play a crucial role in the molecular heat flux reconstruction. LES is conducted either with no SGS-flux model, denoted as 'No SGS' model as already stated, or with SGS-flux models. The flow field ϕ^* obtained from the FC-DNS using M1 is labelled RFC-DNS, where 'R' stands for 'Reconstructed'. When the q-correction is included in an LES, the corresponding label for that LES has HF attached to the model, e.g. SMD HF. To investigate the effect of the q-correction, LES without q-correction are first performed. Then, LES using the same SGS-flux models are conducted, now with the q-correction model M1 using $N = 3$ and filter A. The results are compared with the DNS, and with the FC-DNS or the RFC-DNS.

The comparisons in figure 10(*a*) are for the OH750 case and involve evaluating the x_2-r.m.s. activity of the divergence of the heat flux computed from the filtered flow field of either LES or FC-DNS when no q-correction model is used, as in (2.43). The comparison is with respect to the DNS quantity it aims to reproduce, i.e. $\overline{\nabla \cdot q(\phi)}$. The results show that the target LES solution, FC-DNS, overpredicts the filtered heat flux divergence (the maximum overprediction is 20 % at $x_2/\delta_{\omega,0} = 6$); this is understandable since on the coarse FC-DNS grid the computed gradients will be larger, and it was determined in §6.1.1 that the gradients govern the heat

flux. All LES using SGS-flux models also overpredict the DNS, with the maximum overprediction being approximately 40 % except for the SMD model for which it is 70 % at $x_2/\delta_{\omega,0} = 2$. The heat flux divergence of the No SGS model solution is twice as large as the divergence obtained from the FC-DNS, yielding worse results than any LES using an SGS-flux model, thus indicating the significance of the SGS-flux modelling. Illustrated in figure 10(*b*) is the filtered divergence of the heat flux computed from the reconstructed flow field of either LES or FC-DNS when the LES uses the $\boldsymbol{q}$-correction as in (2.44); this quantity is also compared to the DNS-extracted quantity it means to reproduce, i.e. $\overline{\nabla \cdot \boldsymbol{q}(\phi)}$. Figures 10(*a*) and 10(*b*) are plotted at the same scale to facilitate the comparison between models without and with $\boldsymbol{q}$-correction. When implementing the $\boldsymbol{q}$-correction one computes the divergence of the heat flux from the reconstructed flow field, ϕ^*, instead of the LES or FC-DNS flow field. This leads to a better heat flux divergence approximation as the $\boldsymbol{q}$-correction model shifts the FC-DNS curve to the RFC-DNS which practically coincides with the DNS, with less than 1 % discrepancy (figure 10*b*). Additionally, when the $\boldsymbol{q}$-correction is employed, a clear improvement is exhibited in the x_2-r.m.s. values of the filtered heat flux divergence for all LES, including the No SGS model case, as all LES better predict the filtered DNS heat flux divergence than the LES of figure 10(*a*). The remarkable improvement of the predictions even in the absence of SGS-flux model indicates that the $\boldsymbol{q}$-correction model has the ability to insert considerable SGS activity into the LES equations. In fact, with the exception of the SMD model overprediction, within the layer all SGS-flux models predict values that almost coincide with $\overline{\nabla \cdot \boldsymbol{q}(\phi)}$, with the best prediction within the layer being obtained with the MGRD model.

Complementing the information in figure 10, displayed in figure 11(*a*) is the x_2-r.m.s. of $(\overline{\nabla \cdot \boldsymbol{q}(\phi)} - \nabla \cdot \boldsymbol{q}(\overline{\phi}))$, where $\overline{\phi}$ is either the LES or the FC-DNS flow field for LES devoid of the $\boldsymbol{q}$-correction. Correspondingly exhibited in figure 11(*b*) is the x_2-r.m.s. of $(\overline{\nabla \cdot \boldsymbol{q}(\phi)} - \overline{\nabla \cdot \boldsymbol{q}(\phi^*)})$, where ϕ^* is the reconstructed flow field of either LES or FC-DNS for LES conducted with $\boldsymbol{q}$-correction. Each of these quantities represents the difference between the value that should have entered (2.3) according to the ideal LES based on the DNS and the value that has actually been used. The goal of SGS modelling is to minimize $(\overline{\nabla \cdot \boldsymbol{q}(\phi)} - \nabla \cdot \boldsymbol{q}(\overline{\phi}))$ by using SGS-flux models and to minimize $(\overline{\nabla \cdot \boldsymbol{q}(\phi)} - \nabla \cdot \boldsymbol{q}(\phi^*))$ by utilizing the combination of SGS-flux and $\boldsymbol{q}$-correction models. The effectiveness of the $\boldsymbol{q}$-correction model is measured by the reduction in magnitude from $(\overline{\nabla \cdot \boldsymbol{q}(\phi)} - \nabla \cdot \boldsymbol{q}(\overline{\phi}))$ to $(\overline{\nabla \cdot \boldsymbol{q}(\phi)} - \nabla \cdot \boldsymbol{q}(\phi^*))$. For figure 11(*a*), since the LES is conducted without $\boldsymbol{q}$-correction, the evaluated difference represents the neglected $\boldsymbol{q}$-correction contribution in (2.3) according to either the FC-DNS or the LES solution; for figure 11(*b*), since the LES is conducted with $\boldsymbol{q}$-correction, the computed quantity measures the deficit, despite $\boldsymbol{q}$-correction modelling, between the ideal LES heat flux according to the DNS and that included according to either the RFC-DNS or the LES solution. Moreover, in both figures 11(*a*) and 11(*b*) we present, for comparison, the x_2-r.m.s. of $\overline{\nabla \cdot \boldsymbol{q}(\phi)}$ computed from the DNS and note that it does not correspond to the quantity stated on the ordinate axis. The ordinate non-dimensionalization is such that the x_2-r.m.s. of $\overline{\nabla \cdot \boldsymbol{q}(\phi)}$ reaches a maximum of unity. Clearly, without $\boldsymbol{q}$-correction, the smallest neglected SGS contribution is that of the FC-DNS, which is still substantial at a maximum of 35 % of the ideal $\overline{\nabla \cdot \boldsymbol{q}(\phi)}$. At the other extreme of deviation from the ideal $\overline{\nabla \cdot \boldsymbol{q}(\phi)}$ is the No SGS model for which the neglected SGS contribution is as large as a factor of 1.85 of the filtered DNS heat flux; an overestimate is indeed expected since without the dissipative effect of the SGS-flux models, gradients are larger, and as shown above, the gradients govern the heat flux. With an SGS-flux model, this factor is reduced to a maximum
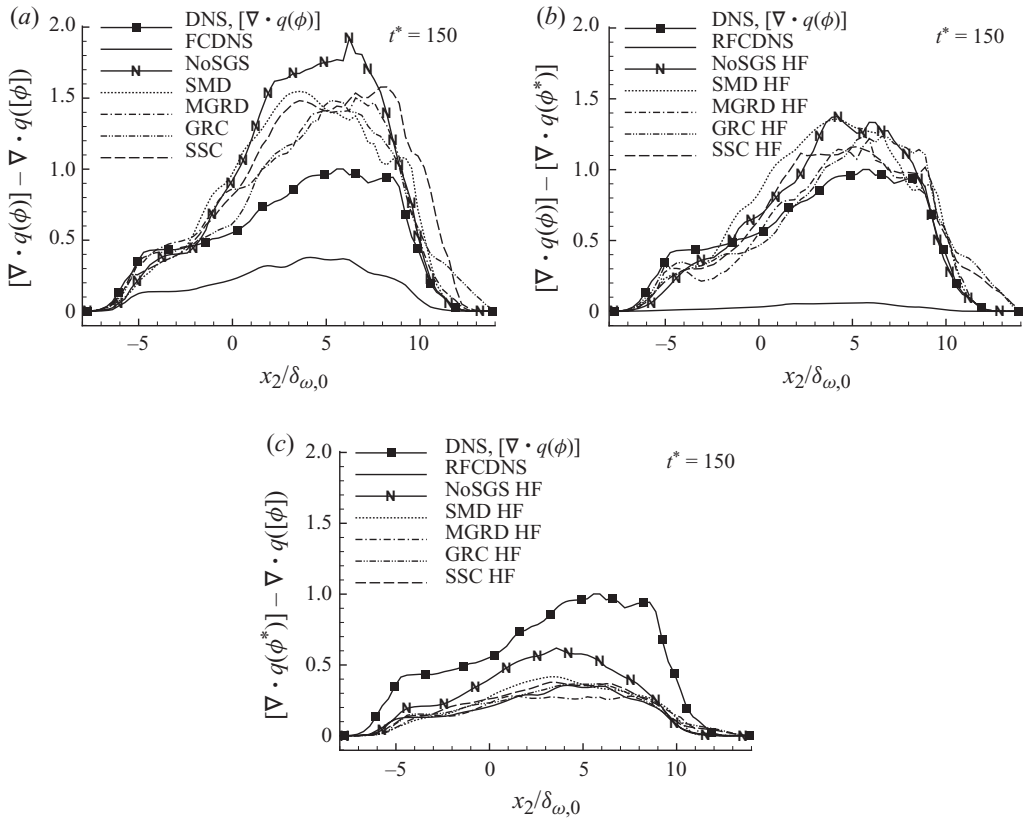
FIGURE 11. The x_2-r.m.s. of several quantities. (*a*) The difference between the filtered divergence of the (coarsened) DNS heat flux and the divergence of the heat flux computed from the filtered flow field of LES or FC-DNS; the LES is without heat flux correction. (*b*) The difference between the filtered divergence of the heat flux computed from the (coarsened) DNS heat flux and the filtered divergence of the reconstructed heat flux using the filtered flow field of either LES or the FC-DNS; the LES is with heat flux correction. (*c*) The difference between the filtered divergence of the reconstructed heat flux and the heat flux computed from the filtered flow field of either LES or FC-DNS; the LES is with heat flux correction. The LES with heat flux correction is denoted by HF and is obtained using model M1. The LES use various SGS-flux models, all defined in §2.4.1. All results are displayed at $t_{tr}^* = 150$. The computations were performed using the O_2/H_2 DNS with $\bar{\Delta} = 8\Delta x_{DNS}$. The values shown are non-dimensionalized by 6.5×10^{10} J m^{-3} s^{-1}. The filtering operation is denoted by square brackets.

of 1.5 of the filtered DNS heat flux. The SGS-flux model for which the neglected quantity is smallest is the GRC model, presumably because its essence is to focus on reconstruction through gradient computation, but even the GRC-model LES is only slightly closer to the FC-DNS than those with other SGS-flux models. Thus, without q-correction, the neglected value is as much as 1.5–1.85 larger than the filtered DNS heat flux. With the q-correction, the divergence discrepancy computed using the RFC-DNS is almost null, which fulfils the best expectation one may have, and that of the No SGS model is reduced from the maximum of 1.85 to as much as a factor of 1.3. When an SGS-flux model is used, the overestimate is reduced to a maximum factor of 1.2 for the MGRD model, which is the model having the smallest discrepancy. This means that although the model $\overline{\nabla \cdot q(\phi^*)}$ for $\overline{\nabla \cdot q(\phi)}$ is very accurate, as shown

in figure 10(*b*), in LES with any SGS-flux model and even including the *q*-correction, the activity of the SGS heat flux discrepancy exceeds that of the ideal filtered heat flux, $\overline{\nabla \cdot \boldsymbol{q}(\phi)}$.

According to statement (2.44), $(\overline{\nabla \cdot \boldsymbol{q}(\phi^*)} - \nabla \cdot \boldsymbol{q}(\overline{\phi}))$ plotted in figure 11(*c*) represents the correction term added to (2.3) using the *q*-correction model. Examination of the results illustrated in figure 11(*c*) indicates that with the implementation of the *q*-correction in LES and the utilization of the reconstructed LES flow field for heat flux computation, this SGS heat-flux divergence difference is similar to that of the RFC-DNS for all SGS-flux models (with the exception of the No SGS model case for which it is larger). This is the best that could be hoped and indicates that this remaining error is irreducible for the SGS heat-flux divergence difference, as also implied by the results of figure 10(*b*).

It is thus clear that $\overline{\nabla \cdot \boldsymbol{q}(\phi^*)}$, where ϕ^* is the reconstructed flow field from LES including an SGS-flux model and the *q*-correction, is a much better approximation of the filtered DNS heat flux divergence, $\overline{\nabla \cdot \boldsymbol{q}(\phi)}$, than is $\nabla \cdot \boldsymbol{q}(\phi_{LES})$ computed from a LES which does not include the *q*-correction model (compare figures 10*a* and 10*b*).

6.2.2. *Effect of the q-correction on flow-variable means, fluctuations and second-order correlations*

So far, the focus has been on the molecular heat flux prediction and it was shown that irrespective of the employed SGS model, the proposed *q*-correction method improves the LES heat flux prediction. It is though also of interest to examine whether the effect of *q*-correction additionally improves the prediction of flow variables. For this purpose, the SGS model most sensitive to the *q*-correction according to the above OH750 analysis – MGRD – is selected and LES for the OH750 case, with or without *q*-correction (MGRDHF or MGRD No HF, respectively) are compared. Comparisons are first conducted for the timewise variation and then for the spatial variation at the transitional time ($t_{tr}^* = 150$). The time variations are obtained by integrating the homogeneous-plane means for each flow variable in the non-homogenous x_2-direction. For any variable A, fluctuations are computed either as $A' = A - \langle A \rangle$, or for Favre-averaged quantities $\{A\} = \langle \rho A \rangle / \langle \rho \rangle$ as $A'' = A - \{A\}$.

Figure 12 illustrates the time variation of non-dimensionalized quantities representing the evolution of $\{T\}$, $\langle p \rangle$, $\{T''\}$, $\langle p' \rangle$, $\langle \rho' \rangle$ and $\{Y_2''\}$. Except for $\langle p \rangle$ and $\langle p' \rangle$ which exhibit improvement over most of or over the entire history, respectively, with the addition of the *q*-correction (figure 12*b*, *d*), the other variables' variation does not benefit from the *q*-correction by comparison with the FC-DNS template, other than towards the end of the calculation when the corresponding prediction improves with respect to the computation devoid of *q*-correction, now reaching towards the FC-DNS. This is particularly pronounced for $\{T\}$ and $\{T''\}$ (figure 12*a*, *c*) which show that the addition of the *q*-correction causes $\{T\}$ to increase and $\{T''\}$ to decrease. It is conjectured that the less favourable agreement of MGRDHF with the FC-DNS than MGRD No HF, except towards the end of the simulation, is due to the lack of strong HDGM regions before that time, invalidating the need for *q*-correction. However, the positive impact of the *q*-correction over the $\langle p \rangle$ and $\langle p' \rangle$ timewise prediction foretells of corresponding improvements in the velocity field that are explored below.

To check whether the *q*-correction indeed beneficially affects the solution at the transitional state, the variables examined in figure 12 are now spatially assessed versus the non-homogeneous direction at $t_{tr}^* = 150$ in figure 13. Although the positive effect of *q*-correction is subtle for $\{T\}$, $\langle p \rangle$ and $\{T''\}$ (figure 13*a–c*, respectively), it is
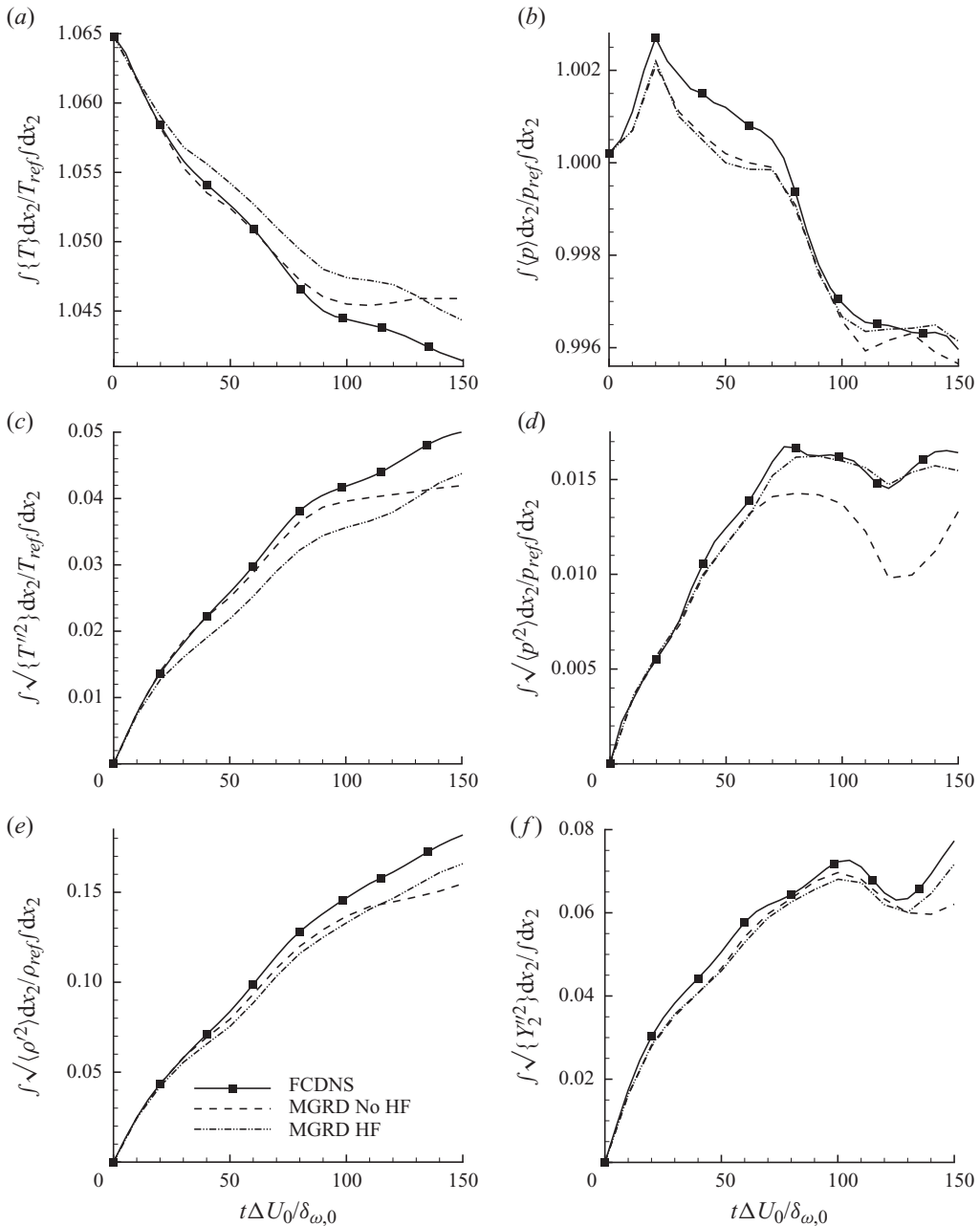
FIGURE 12. Timewise evolution of non-dimensionalized x_2-r.m.s. quantities. (*a*) Mean temperature, (*b*) mean pressure, (*c*) temperature fluctuations, (*d*) pressure fluctuations, (*e*) density fluctuations and (*f*) mass fraction fluctuations. Comparisons are performed among FC-DNS, MGRD without $\boldsymbol{q}$-correction (MGRD No HF) and MGRD with $\boldsymbol{q}$-correction (MGRDHF). $\Delta x_{LES} = 4\Delta x_{DNS}$; $\rho_{ref} = (\rho_1 + \rho_2)/2$, $T_{ref} = (T_1 + T_2)/2$ and $p_{ref} = p_0$.

definitely discernible for $\langle p' \rangle$, $\langle \rho' \rangle$ and $\{Y_2''\}$ (figure 13*d*–*f*, respectively), particularly for $\langle p' \rangle$ and $\{Y_2''\}$ for which substantial improvement is observed.

Since the fluctuation part of the velocity field imparts to a turbulent flow its character, in figure 14 both timewise (figure 14*a*, *c*, *e*) and spatial variations
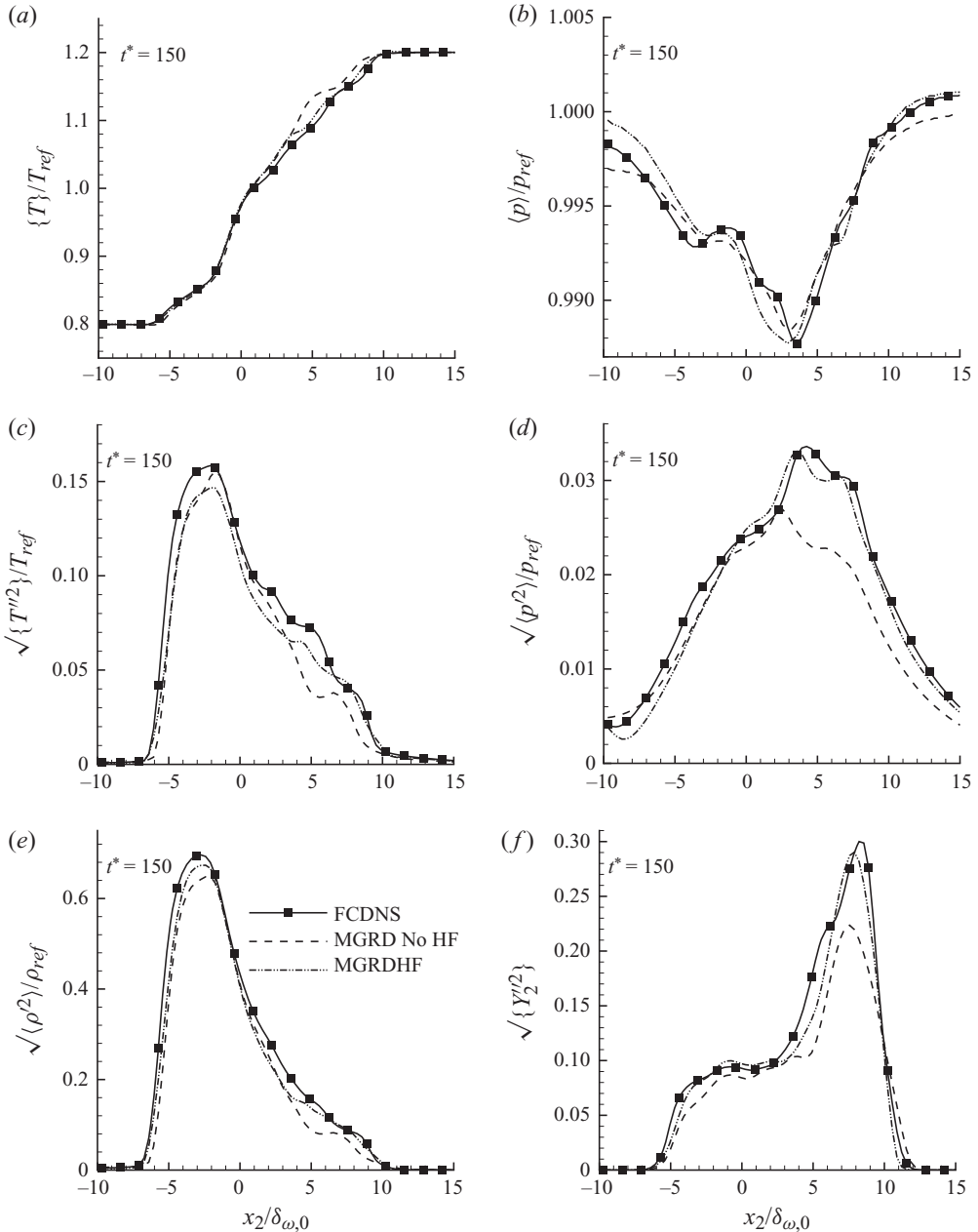
FIGURE 13. Cross-stream variation of non-dimensionalized x_2-r.m.s. quantities at $t_{tr}^* = 150$. (a) Mean temperature, (b) mean pressure, (c) temperature fluctuations, (d) pressure fluctuations, (e) density fluctuations and (f) mass fraction fluctuations. Comparisons are performed among FC-DNS, MGRD without $\boldsymbol{q}$-correction (MGRD No HF) and MGRD with $\boldsymbol{q}$-correction (MGRDHF). $\Delta x_{LES} = 4 \Delta x_{DNS}$; $\rho_{ref} = (\rho_1 + \rho_2)/2$, $T_{ref} = (T_1 + T_2)/2$ and $p_{ref} = p_0$.

(figure 14b,d,f) are displayed for each u_1, u_2 and u_3 fluctuations. Clearly, with the $\boldsymbol{q}$-correction an amelioration of temporal quantity prediction is obtained especially at the later times of the layer evolution, consistent with the development of strong HDGM regions at those times. Noteworthy, for this LES the velocity field benefits more than
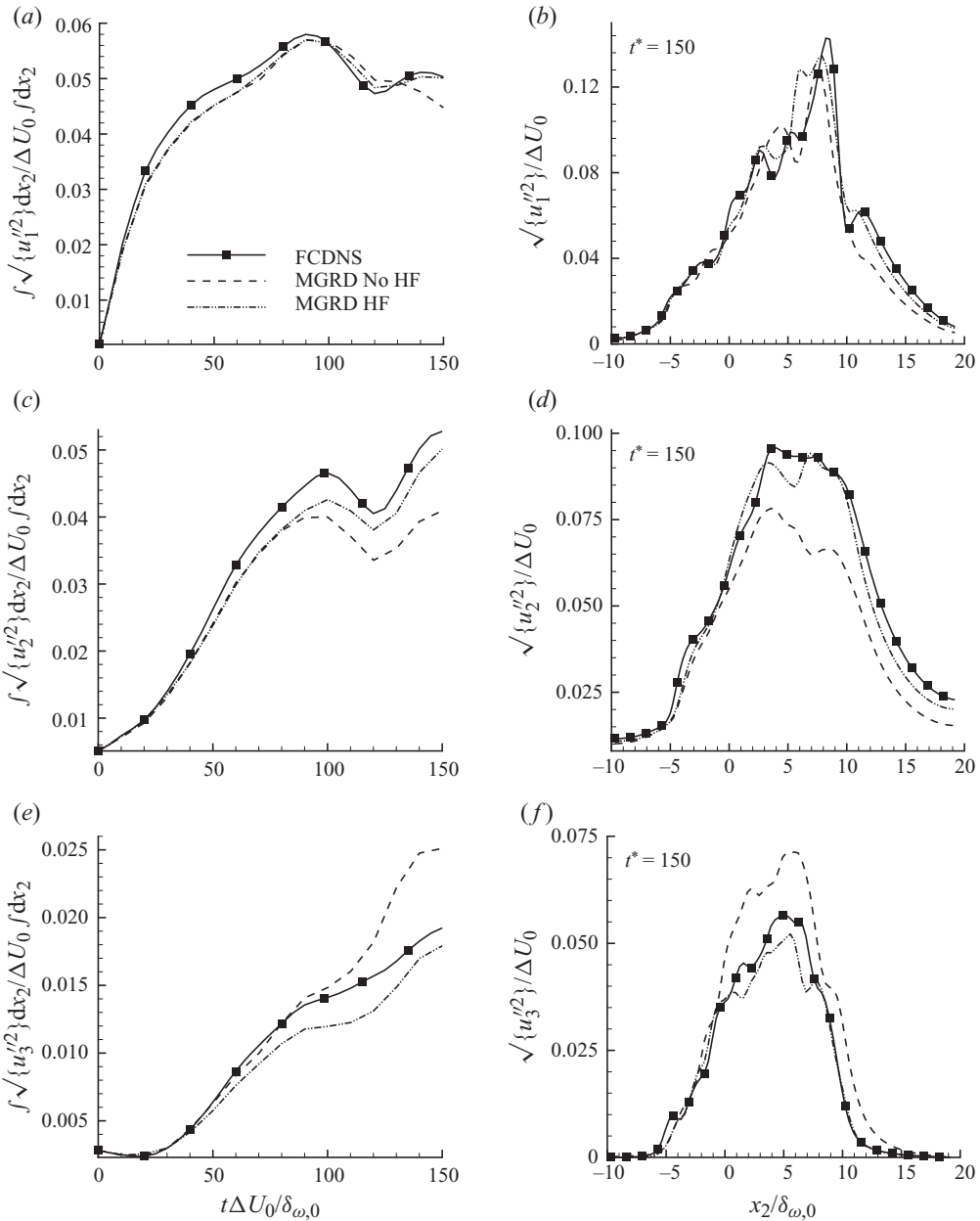
FIGURE 14. Timewise evolution of non-dimensionalized x_2-r.m.s. quantities: (*a*) u_1 velocity fluctuations, (*c*) u_2 velocity fluctuations and (*e*) u_3 velocity fluctuations. Cross-stream variation of x_2-r.m.s velocity fluctuations at $t_{tr}^* = 150$ for (*b*) u_1, (*d*) u_2 and (*f*) u_3. Comparisons are performed among FC-DNS, MGRD without $\boldsymbol{q}$-correction (MGRD No HF) and MGRD with $\boldsymbol{q}$-correction (MGRDHF); $\Delta x_{LES} = 4\Delta x_{DNS}$.

the thermodynamic variables (figure 12) from the $\boldsymbol{q}$-correction. The inclusion of the $\boldsymbol{q}$-correction also enables LES to capture the spatial variation of velocity fluctuations at $t_{tr}^* = 150$ with a dramatic recovery of the FC-DNS template particularly in the cross-stream and spanwise directions. Without $\boldsymbol{q}$-correction, the fluctuating u_2 velocity

is underestimated whereas the fluctuating u_3 velocity is overestimated, which could partially conceal in turbulent kinetic energy calculations the effect of *q*-correction.

Finally, the spatial variation of second-order correlations is scrutinized including the Reynolds stresses, $\langle \rho u_1'' u_2'' \rangle$, $\langle \rho u_3'' u_3'' \rangle$, and correlations between dynamic and thermodynamic variables $\langle \rho u_1'' Y_2'' \rangle$, $\langle \rho u_2'' Y_2'' \rangle$, $\langle \rho u_1'' T'' \rangle$ and $\langle \rho u_2'' T'' \rangle$; the results are displayed in figure 15. All second-order correlations substantially benefit from the *q*-correction, but most considerably those involving u_2 (figure 15*b,d,f*). Since recovery of the second-order correlations is at the heart of turbulence modelling, it is clear that the *q*-correction considerably improves the accuracy of supercritical LES computations.

6.2.3. *Effect of the q-correction on flow variable visualizations*

To illustrate the effect of the *q*-correction model on flow visualizations, the OHe600 case is selected because at the same momentum flux ratio, $(\rho_2 U_2^2 / \rho_1 U_1^2) \sim 1$, it achieves a 25 % higher value of $Re_{m,tr}$ (see table 3) than the OH750 case and thus the results are slightly more relevant to fully turbulent flows.

To assess the influence of the *q*-correction model for the OHe600, selected LES were performed without and with the M1 *q*-correction model, and they were compared to the FC-DNS. Results are displayed in figures 16 and 17 for the SMD and MGRD SGS-flux models, respectively. The comparisons are made for $|\nabla \rho|$ because the structure of the HDGM regions crucially affects turbulence distribution in the flow field (Hannoun *et al.* 1988), p/p_0 because of the strong coupling among thermodynamic quantities through the EOS and because the accurate p prediction governs that of the velocity field, Y_o because it is a manifestation of mixing, and T because it is intertwined with *q*.

Considering figure 16 and comparing the results of the LES using the SMD model devoid of *q*-correction model with the FC-DNS template, it appears that the former is unable to accurately reproduce the HDGM regions of the FC-DNS, even though these regions do not exhibit much small-scale structure. In this LES, the p field is overpredicted in that regions of either small or large p are enlarged, and the detailed structure of both Y_o and T inside the vortex is missed although the size of the vortex is reasonably well captured. The LES including the *q*-correction model is no more successful than that devoid of this *q*-correction model in recovering the structure of the FC-DNS, indicating that the overdissipative deficiency of the SMD model cannot be palliated by the *q*-correction model since the ADM reconstruction is SGS-flux model dependent, as stated in §2.4.2.

As shown in figure 17, when using the MGRD model alone, without the *q*-correction, the LES mispredicts all spatial distributions of $|\nabla \rho|$, p/p_0, Y_o and T. The spatial extent of the HDGM regions is overpredicted, the relative placement of the low and high p regions is incorrect, the size of the vortex is reduced with respect to that of the FC-DNS and as a result the Y_o and T fields are incorrect. Including the *q*-correction model in LES enlarges the vortex size, although it is still somewhat reduced with respect to that of the FC-DNS, leads to a much better representation of the HDGM regions, redresses the incorrect relative placement of the low and high p regions although all details of the FC-DNS are still not captured, and improves the Y_o and T distributions, although the entire structure of the template is still not well reproduced.

Given the lack of predictive capability of the LES using the SMD model whether devoid of or in conjunction with the *q*-correction model, and the serious deficiencies of the LES utilizing the MGRD model without *q*-correction, by elimination, the LES utilizing the MGRD model and including the *q*-correction seems the most promising.
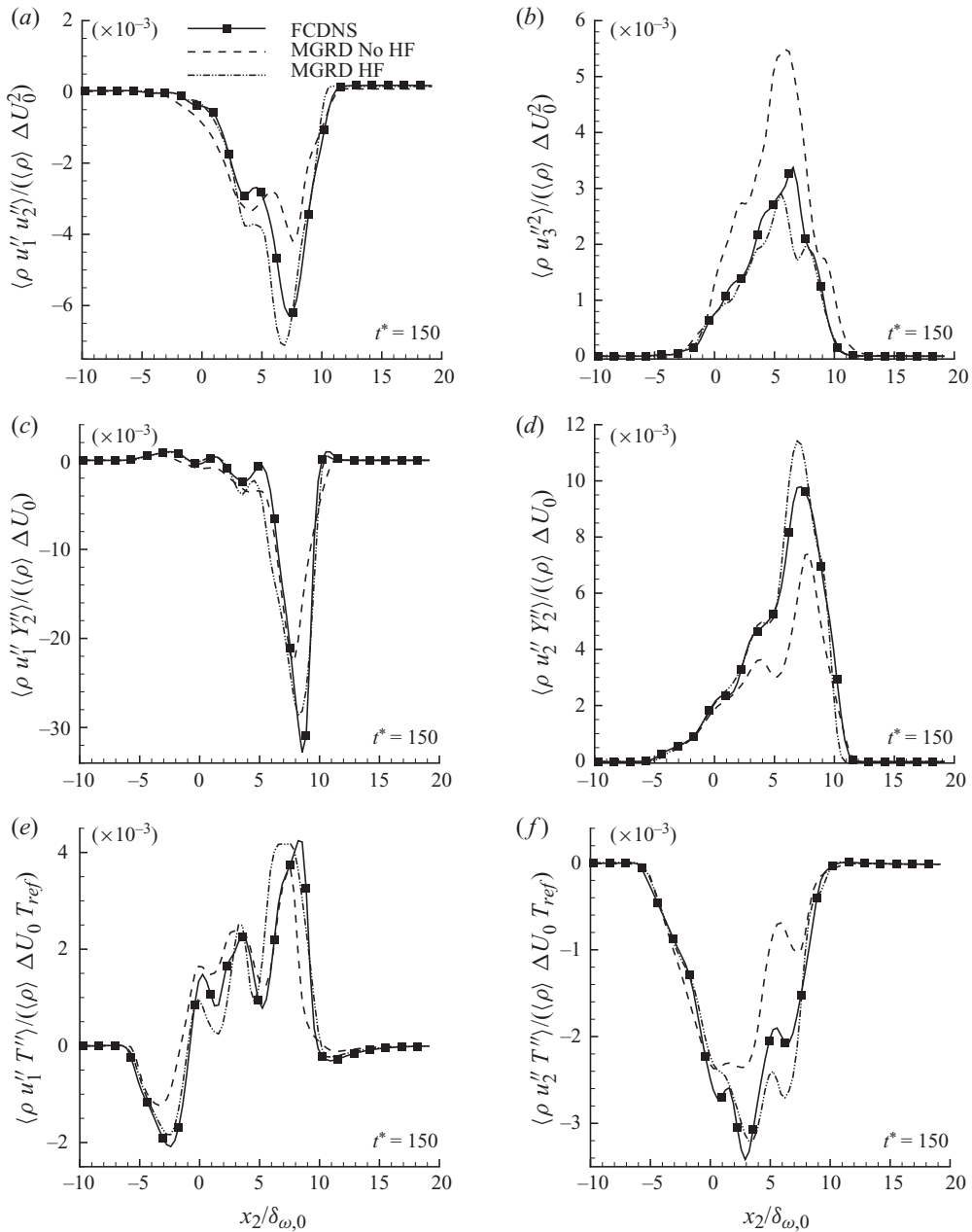
FIGURE 15. Cross-stream variation of non-dimensional second-order correlations at $t_{tr}^* = 150$ (a) $\langle \rho u_1'' u_2'' \rangle$, (b) $\langle \rho u_3'' u_3'' \rangle$, (c) $\langle \rho u_1'' Y_2'' \rangle$, (d) $\langle \rho u_2'' Y_2'' \rangle$, (e) $\langle \rho u_1'' T'' \rangle$ and (f) $\langle \rho u_2'' T'' \rangle$. Comparisons are performed among FC-DNS, MGRD without q-correction (MGRD No HF) and MGRD with q-correction (MGRDHF). $\Delta x_{LES} = 4 \Delta x_{DNS}$, $T_{ref} = (T_1 + T_2)/2$.

7. Summary and conclusions

A priori and *a posteriori* studies were both here conducted to identify the necessary SGS models in LES for predicting counterflow fluid motion, disintegration and mixing of either oxygen/hydrogen streams or oxygen/helium streams at an initial pressure
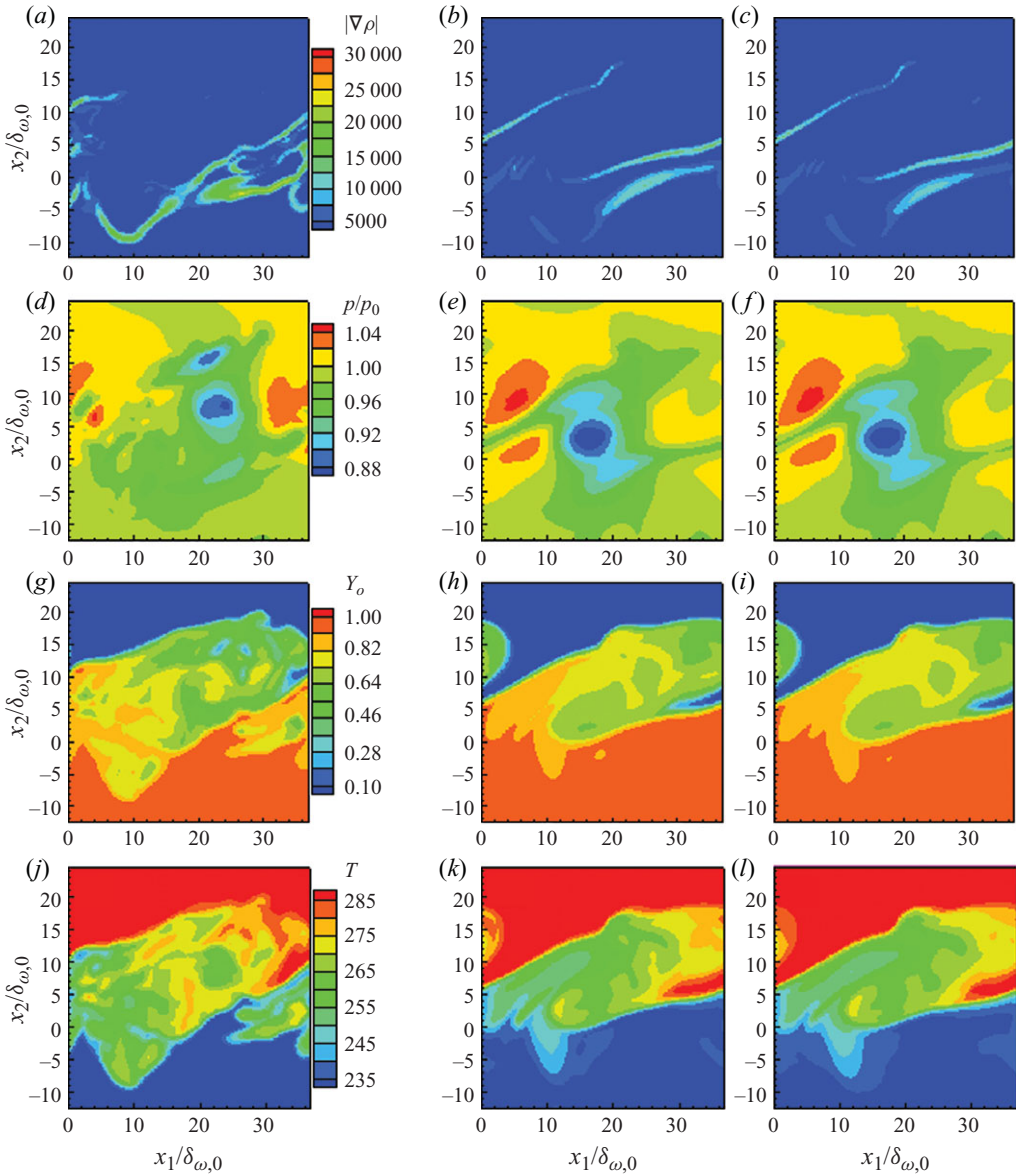
FIGURE 16. Comparison of $|\nabla\rho|$ in $kg\,m^{-4}$ (*a–c*), p/p_0 (*d–f*) and Y_o (*g–i*) and T in K (*j–l*) for the O_2/He layer at the t_{tr}^* of the DNS ($t^* = 220$) in the between-the-braid plane ($x_3/L_3 = 0.06$) for FC-DNS (*a,d,g,j*), SMD without $\boldsymbol{q}$-correction (*b,e,h,k*) and SMD with $\boldsymbol{q}$-correction (*c,f,i,l*). $\Delta x_{LES} = 4\Delta x_{DNS}$.

higher than the critical pressure of these fluids. The LES governing equations consist of the filtered original equations for conservation of mass, momentum, species and total energy coupled with a real-gas EOS; these equations were previously solved using DNS with transport properties which were functions of the thermodynamic variables. Identified in a previous *a priori* investigation (Selle *et al.* 2007), for these fluids, the SGS terms in the filtered differential equations consist of two types: (i) the typical SGS-flux terms and (ii) a heat-flux correction in the energy equation accounting for
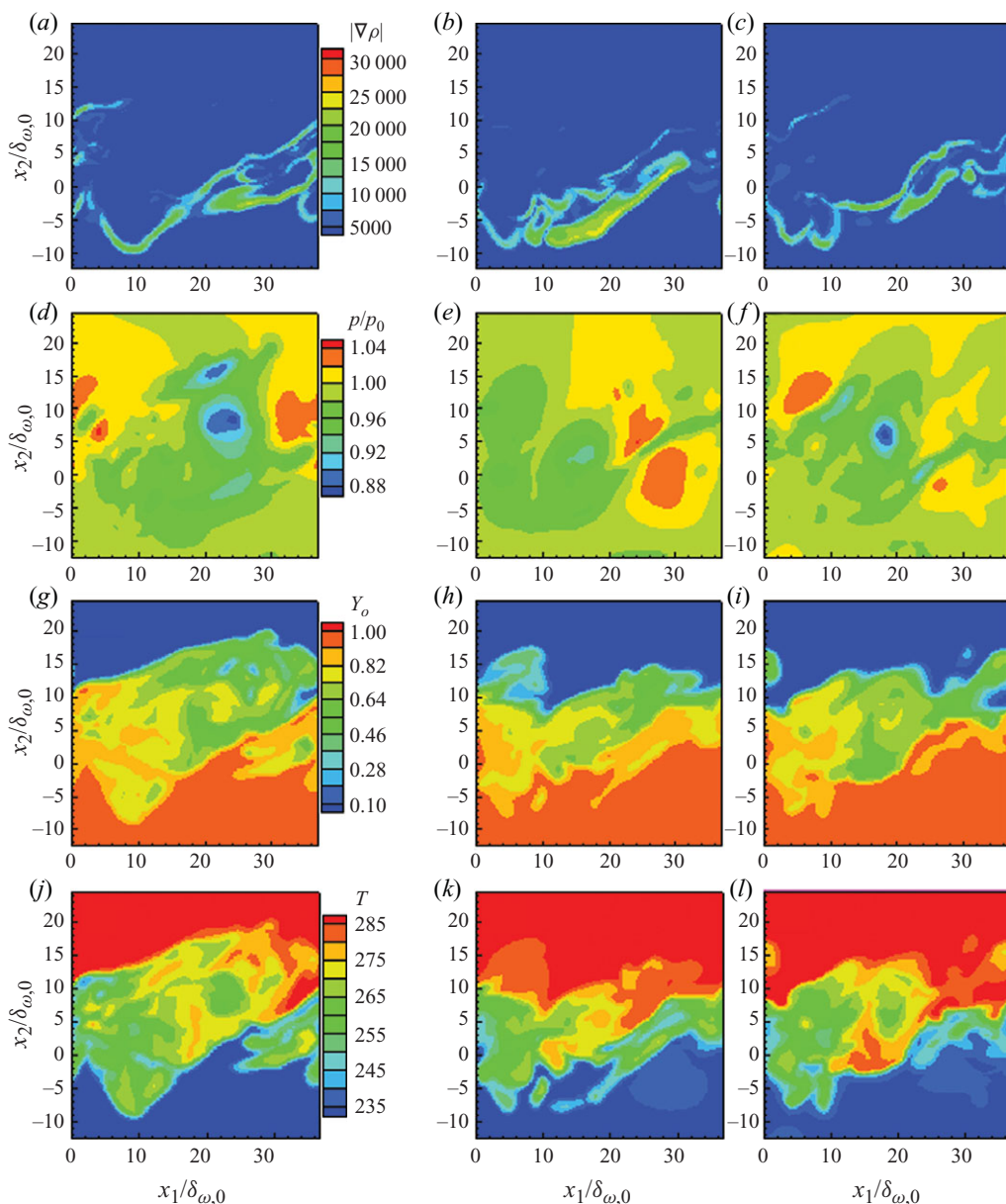
FIGURE 17. Comparison of $|\nabla \rho|$ in $kg\,m^{-4}$ (a–c), p/p_0 (d–f) and Y_o (g–i) and T in K (j–l) for O_2/He at the t_{tr}^* of the DNS ($t^* = 220$) in the between-the-braid plane ($x_3/L_3 = 0.06$) for FC-DNS (a, d, g, j), MGRD without $\boldsymbol{q}$-correction (b, e, h, k) and MGRD with $\boldsymbol{q}$-correction (c, f, i, l). $\Delta x_{LES} = 4\Delta x_{DNS}$.

the difference between the filtered divergence of the molecular heat flux computed using the DNS flow field and the divergence of the molecular heat flux computed from the filtered flow field. The second type of SGS term is the direct result of the strong coupling between the flow dynamics represented by the differential governing equations and the fluid thermodynamics represented by the highly nonlinear EOS.

This coupling manifests through the appearance of HDGM regions having either a filamentary or blob-like aspect.

The configuration was that of a three-dimensional mixing layer with initially oxygen in the lower stream and either hydrogen or helium in the upper stream, and the DNS followed, for each realization, the evolution of the layer from an initial laminar state to a transitional state. The LES were carried out with the same numerical discretization and time advancement numerical scheme as the DNS. Both LES were conducted up to the same non-dimensional simulation time as the respective DNS using the filtered DNS initial conditions. In both cases, the LES grid volume was 64 times larger than the DNS grid volume.

In the *a priori* study, we identified the primitive variable gradients, rather than their associated coefficients, as controlling both the heat flux value and its spatial variation. This indicated that the focus should be on reconstructing these gradients from the filtered flow field rather than the coefficients as previously done by Selle *et al.* (2007). Among the three contributions to the heat flux due to temperature, species mass fraction and pressure gradients, the gradients due to species non-uniformities were by far the most important contribution to the heat flux; it was conjectured that the relative importance of these contributions may change in situations in which the initial temperature difference between free streams is larger than that constrained in the present DNS by the necessity to resolve the initial density gradient in the vorticity thickness layer. Several models were proposed for the gradient reconstruction and the success in this endeavour was checked by comparing the results to the filtered-and-coarsened DNS (FC-DNS), which is considered the LES template. Additionally, analyses for the selection of the reconstruction filter mathematical form and reconstruction order were conducted, leading to the choice of the ADM (Stolz & Adams 1999) using a reconstruction order of 3 for the *a posteriori* study. With this model, the *a priori* analysis showed that the SGS molecular heat-flux difference can be improved by as much as 60 %. It was also shown that as the filter-to-grid ratio increases, the importance of the heat-flux correction term with respect to the resolved heat flux increases.

The *a posteriori* LES tests were performed without or with the heat-flux correction model. Because the heat-flux correction model is computed from an LES with a specified SGS-flux model (which also encompasses a null SGS-flux model), the result of the heat-flux correction was intertwined with that of the typical SGS-flux model. The LES were conducted for the oxygen/hydrogen case with two constant-coefficient (scale-similarity and gradient) SGS-flux models, two dynamic-coefficient (Smagorinsky/Yoshizawa and mixed Smagorinsky/Yoshizawa/gradient) SGS-flux models, and with a null SGS-flux model. For the oxygen/helium case, LES were conducted with two dynamic-coefficient (Smagorinsky/Yoshizawa and mixed Smagorinsky/Yoshizawa/gradient) SGS-flux models either devoid of or including the heat-flux correction model. The results showed that the heat flux representation is indeed improved through the heat-flux correction. For all SGS-flux models, with the exception of the null SGS-flux model, the use of the heat-flux correction through the ADM reconstruction effectively reduced the SGS heat-flux difference to that obtained from a reconstructed FC-DNS, called RFC-DNS, and thus further reduction is theoretically impossible. Examination of timewise and spatial cross-stream r.m.s. variations of variable means, fluctuations and second-order correlations highlighted the beneficial effect of the heat-flux correction. Flow visualizations showed that by elimination, the dynamic-coefficient mixed Smagorinsky/Yoshizawa/gradient SGS-flux model including the heat-flux correction model was the most promising.

Lastly, the methodology of introducing in LES other SGS models than those addressing the SGS fluxes may prove crucial for performing LES for turbulent flow in large geometries for which coarse grids are the only option. For these coarse LES grids, neglected small-scale effects other than the typical SGS fluxes could be considerable and the only way to reintroduce these effects into the LES computation may be through modelling differences between the unknown filtered quantity and the quantity computed in LES (using e.g. ADM). Such models may be necessary not only for the molecular heat flux but also for the pressure gradient in the momentum equation (see Taşkinoğlu & Bellan 2010), for the stresses in the momentum equation, and/or for the work due to pressure or stresses in the energy equation. This strategy may enable LES in situations in which they are currently unpractical because the required grid for acceptable accuracy is too fine for computational efficiency.

Appendix. Transport properties for O_2/He mixtures

For O_2/He mixtures, the Prandtl number is approximated as

$$Pr = 0.68 + 0.0283\xi - 0.5017\xi^2 - 0.5390\xi^3 + \Delta Pr, \tag{A 1}$$

where

$$\xi = \min(0.5, Y_2 - 0.81\theta^{0.35}), \quad \theta = (T - 100)/800, \quad 0 \leqslant \theta \leqslant 1 \ (T \text{ in Kelvin}).$$

For $0.02 \leqslant \theta \leqslant 0.368$, $\Delta Pr = 2.42 Y_2^{14.6} \max(0.0, -0.23(1 + \ln \theta))$, otherwise $\Delta Pr = 0$.

For O_2/He mixtures, the Schmidt number is approximated as

$$\left.\begin{aligned} Sc &= \Sigma(Y_2)[1 + (114/T)^{1.5}]/(1 + \Delta_s), \\ T < 200\,\text{K}: \ \Sigma &= \left(1.292 - 0.757 Y_2 + 0.444 Y_2^2 - 0.757 Y_2^3\right), \\ T > 200\,\text{K}: \ \Sigma &= \left(1.318 - 0.772 Y_2 + 0.453 Y_2^2 - 0.772 Y_2^3\right). \end{aligned}\right\} \tag{A 2}$$

For $p < 30$ MPa, $\Delta_s = \min(0.08, 0.1264 + 0.226 Y_R) + 0.1 \exp(-2400\theta^{4.5})$, where $Y_R = Y_2 - \min(1, 0.5 + 0.78\theta^{0.6})$, otherwise $\Delta_s = 0$.

REFERENCES

BARDINA, J., FERZIGER, J. & REYNOLDS, W. 1980 Improved subgrid scale models for large eddy simulation. *AIAA Paper* 80-1357.

BELLAN, J. 2006 Theory, modeling and analysis of turbulent supercritical mixing. *Combust. Sci. Technol.* **178**, 253–281.

BELLAN, J. & SELLE, L. C. 2009 Large eddy simulation composition equations for single-phase and two-phase fully multicomponent flows. *Proc. Combust. Inst.* **32**, 2239–2246.

CARATI, D., WINCKELMANS, G. S. & JEANMART, H. 2001 On the modelling of the subgrid-scale and filtered-scale stress tensors in large-eddy simulation. *J. Fluid Mech.* **442**, 119–138.

CHEHROUDI, B., TALLEY, D. & COY, E. 1999 Initial growth rate and visual characteristics of a round jet into a sub- to supercritical environment of relevance to rocket, gas turbine and diesel engines. *AIAA Paper* 99-0206.

CHOW, F. K. & P. MOIN, P. 2003 A further study of numerical errors in large-eddy simulations. *J. Comput. Phys.* **184**, 366–380.

CLARK, R., FERZIGER, J. & REYNOLDS, W. 1979 Evaluation of subgrid-scale models using an accurately simulated turbulent flow. *J. Fluid Mech.* **91** (1), 1–16.

GERMANO, M., PIOMELLI, U., MOIN, P. & CABOT, W. 1991 A dynamic subgrid-scale eddy viscosity model. *Phys. Fluids* A **3** (7), 1760–1765.

GEURTS, B. J. 1997 Inverse modeling for large-eddy simulation. *Phys. Fluids* **9** (12), 3585–3587.

GEURTS, B. J. & FROHLICH, J. 2002 A framework for predicting accuracy limitations in large-eddy simulation. *Phys. Fluids* **14** (6), L41–L44.

GHOSAL, S. 1996 An analysis of numerical errors in large-eddy simulations of turbulence. *J. Comput. Phys.* **125**, 187–206.

HANNOUN, I. A., FERNANDO, H. J. S. & LIST, E. J. 1988 Turbulence structure near a sharp density interface. *J. Fluid Mech.* **189**, 189–209.

HARSTAD, K. & BELLAN, J. 1998 Isolated fluid oxygen drop behavior in fluid hydrogen at rocket chamber pressures. *Intl J. Heat Mass Transfer* **41**, 3537–3550.

HARSTAD, K. & BELLAN, J. 2000 An all-pressure fluid-drop model applied to a binary mixture: heptane in nitrogen. *Intl J. Multiphase Flow* **26** (10), 1675–1706.

HARSTAD, K., MILLER, R. S. & BELLAN, J. 1997 Efficient high-pressure state equations. *AIChE J.* **43** (6), 1605–1610.

KEIZER, J., 1987 *Statistical Thermodynamics of Nonequilibrium Processes*. Springer.

KENNEDY, C. & CARPENTER, M. 1994 Several new numerical methods for compressible shear layer simulations. *Appl. Numer. Maths* **14**, 397–433.

LEBOISSETIER, A., OKONG'O, N. & BELLAN, J. 2005 Consistent large-eddy simulation of a temporal mixing layer laden with evaporating drops. Part 2. *A posteriori* modeling. *J. Fluid Mech.* **523**, 37–78.

LILLY, D. 1992 A proposed modification of the Germano subgrid-scale closure method. *Phys. Fluids* A **4** (3), 633–635.

LIU, S., MENEVEAU, C. & KATZ, J. 1994 On the properties of similarity subgrid-scale models as deduced from measurements in a turbulent jet. *J. Fluid Mech.* **275**, 83–119.

MAYER, W., IVANCIC, B., SCHIK, A. & HORNUNG, U. 1998 Propellant atomization in LOX/GH2 rocket combustors. *AIAA Paper* 98-3685.

MAYER, W., SCHIK, A., SCHWEITZER, C. & SCHAFFLER, M. 1996 Injection and mixing processes in high pressure LO_X/GH2 rocket combustors. *AIAA Paper* 96-2620.

MILLER, R., HARSTAD, K. & BELLAN, J. 2001 Direct numerical simulations of supercritical fluid mixing layers applied to heptane–nitrogen. *J. Fluid Mech.* **436**, 1–39.

MOIN, P., SQUIRES, K., CABOT, W. & LEE, S. 1991 A dynamic subgrid-scale model for compressible turbulence and scalar transport. *Phys. Fluids* **3** (11), 2746–2757.

MOSER, R. & ROGERS, M. 1991 Mixing transition and the cascade to small scales in a plane mixing layer. *Phys. Fluids* A **3** (5), 1128–1134.

MOSER, R. & ROGERS, M. 1993 The three-dimensional evolution of a plane mixing layer: pairing and transition to turbulence. *J. Fluid Mech.* **247**, 275–320.

MULLER, S. M. & SCHEERER, D. 1991 A method to parallelize tridiagonal solvers. *Parallel Comput.* **17**, 181–188.

OKONG'O, N. & BELLAN, J. 2002a Direct numerical simulation of a transitional supercritical binary mixing layer: heptane and nitrogen. *J. Fluid Mech.* **464**, 1–34.

OKONG'O, N. & BELLAN, J. 2002b Consistent boundary conditions for multicomponent real gas mixtures based on characteristic waves. *J. Comput. Phys.* **176**, 330–344.

OKONG'O, N. & BELLAN, J. 2003 Real gas effects of mean flow and temporal stability of binary-species mixing layers. *AIAA J.* **41** (12), 2429–2443.

OKONG'O, N. & BELLAN, J. 2004a Turbulence and fluid-front area production in binary-species, supercritical, transitional mixing layers. *Phys. Fluids* **16** (5), 1467–1492.

OKONG'O, N. & BELLAN, J. 2004b Consistent large eddy simulation of a temporal mixing layer laden with evaporating drops. Part 1. Direct numerical simulation, formulation and *a priori* analysis. *J. Fluid Mech.* **499**, 1–47.

OKONG'O, N. & BELLAN, J. 2004c Perturbation and initial Reynolds number effects on transition attainment of supercritical mixing layers. *Comput, Fluids* **33** (8), 1023–1046.

OKONG'O, N., HARSTAD, K. & BELLAN, J. 2002 Direct numerical simulations of O_2/H_2 temporal mixing layers under supercritical conditions. *AIAA J.* **40** (5), 914–926.

OSCHWALD, M. & SCHIK, A. 1999 Supercritical nitrogen free jet investigated by spontaneous Raman scattering. *Exp. Fluids* **27**, 497–506.

OSCHWALD, M., SCHIK, A., KLAR, M. & MAYER, W. 1999 Investigation of coaxial LN2/GH2-injection at supercritical pressure by spontaneous Raman scattering. *AIAA* 99-2887.

PAPAMOSCHOU, D. & ROSHKO, A. 1988 The compressible turbulent shear layer: an experimental study. *J. Fluid Mech.* **197**, 453–477.

POPE, S. B. 2004 Ten questions concerning the large-eddy simulation of turbulent flows. *New J. Phys.* **6**, 35–59.

PRAUSNITZ, J., LICHTENTHALER, R. & DE AZEVEDO, E. 1986 *Molecular Thermodynamics for Fluid-Phase Equilibrium*. Prentice-Hall.

PRUETT, C., SOCHACKI, J. & ADAMS, N. 2001 On Taylor-series expansions of residual stress. *Phys. Fluids* **13** (9), 2578–2589.

SARMAN, S. & EVANS, D. J. 1992 Heat flux and mass diffusion in binary Lennard–Jones mixtures. *Phys. Rev.* **A45** (4), 2370–2379

SEGAL, C. & POLIKHOV, S. 2008 Subcritical to supercritical mixing. *Phys. Fluids* **20**, 052101-7.

SELLE, L. C., OKONG'O, N. A., BELLAN, J. & HARSTAD, K. G. 2007 Modeling of subgrid-scale phenomena in supercritical transitional mixing layers: an *a priori* study. *J. Fluid Mech.* **593**, 57–91.

SMAGORINSKY, J. 1963 General circulation experiments with the primitive equations. Part 1. Basic experiments. *Mon. Weath. Rev.* **91**, 99–164.

SMAGORINSKY, J. 1993 Some historical remarks on the use of nonlinear viscosities. In *Large Eddy Simulation of Complex Engineering and Geophysical Flows* (ed. B. Galperin & S. Orszag), chap. 1, pp. 3–36. Cambridge University Press.

STOLZ, S. & ADAMS, N. A. 1999 An approximate deconvolution procedure for large-eddy simulation. *Phys. Fluids* **11** (7), 1699–1701.

STOLZ, S., ADAMS, N. A. & KLEISER, L. 2001 An approximate deconvolution model for large-eddy simulation with application to incompressible wall-bounded flows. *Phys. Fluids* **13** (4), 997–1015.

TAŞKINOĞLU, E. S. & BELLAN, J. 2010 *A posteriori* study using a DNS database describing fluid disintegration and binary-species mixing under supercritical pressure: heptane and nitrogen. *J. Fluid Mech.* **645**, 211–254.

TENNEKES, H. & LUMLEY, J. L. 1989 *A First Course in Turbulence*. MIT Press.

TUCKER, P. K., MENON, S., MERKLE, C. L., OEFELEIN, J. C. & YANG, V. 2008 Validation of high-fidelity CFD simulations for rocket injector design. *AIAA Paper* 2008-5226, presented at the 44th Joint Propulsion Conference, Hartford, CT.

VREMAN, B., GEURTS, B. & KUERTEN, H. 1995 *A priori* tests of large eddy simulation of the compressible plane mixing layer. *J. Engng Maths* **29**, 299–327.

VREMAN, B., GEURTS, B. & KUERTEN, H. 1996 Large eddy simulation of the temporal mixing layer using the Clark model. *Theor. Comput. Fluid Dyn.* **8**, 309–324.

VREMAN, B., GEURTS, B. & KUERTEN, H. 1997 Large-eddy simulation of the turbulent mixing layer. *J. Fluid Mech.* **339**, 357–390.

YOSHIZAWA, A. 1986 Statistical theory for compressible turbulent shear flows, with the application to subgrid modeling. *Phys. Fluids* **29** (7), 2152–2164.